



**HAL**  
open science

# Layered Sodium Titanium Trichalcogenide $\text{Na}_2\text{TiCh}_3$ Framework (Ch = S, Se): A Rich Crystal and Electrochemical Chemistry

Bernhard Leube, Elodie Salager, Erwan Chesneau, Gwenaëlle Rouse, Hervé Vezin, Artem Abakumov, Jean-Marie Tarascon

► **To cite this version:**

Bernhard Leube, Elodie Salager, Erwan Chesneau, Gwenaëlle Rouse, Hervé Vezin, et al.. Layered Sodium Titanium Trichalcogenide  $\text{Na}_2\text{TiCh}_3$  Framework (Ch = S, Se): A Rich Crystal and Electrochemical Chemistry. *Chemistry of Materials*, 2022, 34 (5), pp.2382-2392. 10.1021/acs.chemmater.1c04374 . hal-03614720

**HAL Id: hal-03614720**

**<https://hal.univ-lille.fr/hal-03614720v1>**

Submitted on 21 Nov 2022

**HAL** is a multi-disciplinary open access archive for the deposit and dissemination of scientific research documents, whether they are published or not. The documents may come from teaching and research institutions in France or abroad, or from public or private research centers.

L'archive ouverte pluridisciplinaire **HAL**, est destinée au dépôt et à la diffusion de documents scientifiques de niveau recherche, publiés ou non, émanant des établissements d'enseignement et de recherche français ou étrangers, des laboratoires publics ou privés.

# The layered sodium titanium trichalcogenide $\text{Na}_2\text{TiCh}_3$ framework ( $\text{Ch} = \text{S}, \text{Se}$ ): A rich crystal and electrochemical chemistry.

Bernhard T. Leube<sup>1,2</sup>, Elodie Salager<sup>2,3</sup>, Erwan Chesneau<sup>2,3</sup>, Gwenaëlle Rousse<sup>1,2,4</sup>, Hervé Vezin<sup>5</sup>, Artem M. Abakumov<sup>6</sup> and Jean-Marie Tarascon<sup>1,2</sup>

<sup>1</sup> Collège de France, Chaire de Chimie du Solide et de l'Energie, UMR 8260, 11 Place Marcelin Berthelot, 75231 CEDEX 05 Paris, France

<sup>2</sup> Réseau sur le Stockage Electrochimique de l'Energie (RS2E), FR CNRS 3459, 33 Rue Saint Leu, 80039 Amiens, France

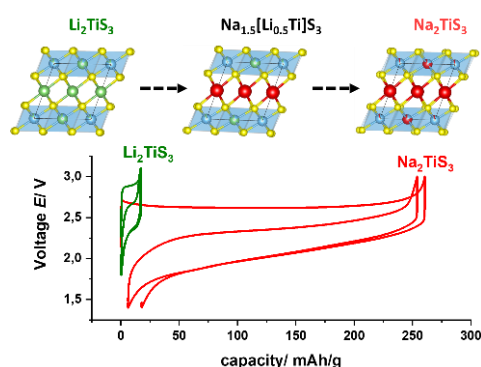
<sup>3</sup> CNRS, CEMHTI, UPR3079, Université d'Orléans, 1D avenue de la recherche scientifique, Orléans, France

<sup>4</sup> Sorbonne Université, 4 Place Jussieu, F-75005 Paris, France

<sup>5</sup> Université Lille Nord de France, CNRS UMR8516, LASIRE, Villeneuve d'Ascq, France

<sup>6</sup> Center for Energy Science and Technology, Skolkovo Institute of Science and Technology, Nobel str. 3, 121205 Moscow, Russia

## Abstract:



The synthesis and characterization of novel alkaline rich transition metal chalcogenides is an intriguing task for solid-state chemists and battery researchers. This class of materials allures by its rich compositional variety, high theoretical capacities and sometimes surprising electrochemistry. Using electrochemically inactive O3-type  $\text{Li}_2\text{TiS}_3$  as a starting point, we embark on the synthesis and electrochemical characterization of five novel chalcogenides:  $\text{Na}_2\text{TiS}_3$ ,  $\text{Na}_2\text{TiSe}_3$ ,  $\text{Na}_2\text{ZrS}_3$ ,  $\text{Na}_2\text{ZrSe}_3$  and finally  $\text{Na}_{1.5}[\text{Li}_{0.5}\text{Ti}]\text{S}_3$ . All compounds crystallize in the layered O3 structure type, but show different electrochemical activity. In particular  $\text{Na}_2\text{TiS}_3$  proves to be an interesting cathode material: the exchange of Li for Na unlocks electrochemical activity and allows for sustained electrochemical cycling of up to 1.8 Na per formula unit. We elucidate the structural evolution of the  $\text{Na}_x\text{TiS}_3$  framework during cycling and find a reversible structural transformation from O3 to O1 stacking of the  $\text{TiS}_3$  octahedral layers. These findings could help to understand the origin of anionic redox activity in the materials based on  $d^0$  transition metals while opening another direction towards cathode materials comprising solely abundant elements.

## Introduction

Li-ion batteries have emerged as the predominant solution for the storage of electric energy. However, new concepts of electroactive materials are needed to further push energy density, reduce costs and

improve safety and sustainability. As a viable substitute, Na-ion battery technology gains increased attention due to high abundance of sodium and perceived similarity to the highly developed Li-ion systems.

In analogy to O3-type (Delma's notation)<sup>1</sup> Li-rich layered oxides (*e.g.*  $\text{Li}_2\text{IrO}_3$ ,  $\text{Li}_2\text{RuO}_3$ ,  $\text{Li}_2\text{MnO}_3$ ),<sup>2-4</sup> one could envisage the development of isostructural Na-rich cathode materials. However, only handful well characterized Na-rich O3-type oxides are known so far ( $\text{Na}_2\text{RuO}_3$ ,  $\text{Na}_2\text{ZrO}_3$ ,  $\text{Na}_2\text{IrO}_3$ )<sup>5-7</sup> - in particular stoichiometric 3d metal based materials are rare. The size mismatch between the  $\text{NaO}_6$  and  $\text{MO}_6$  octahedra coupled with a propensity of Na for prismatic coordination, favors crystallization of many compositions in the non-stoichiometric P2 structure type ( $\text{Na}_x\text{A}_y\text{TM}_{1-x}\text{O}_2$  (A= alkaline metal, TM= transition metal;  $0 < x < 1$ ,  $y < 1$ )). In search for sodium-rich phases, our group recently presented the mixed  $\text{Na}_{1.5}\text{Li}_{0.5}\text{IrO}_3$  and  $\text{Na}_{1.5}\text{Li}_{0.5}\text{MnO}_3$  O3-type phases, in which layers are formed by  $\text{NaO}_6$  and mixed (Li/TM) $\text{O}_6$  octahedra. The strategy of partially substituting Li for Na alleviates the problems associated with the size mismatch in the mixed (A/TM) $\text{O}_6$  layer.<sup>8,9</sup>

Another angle towards sodium-rich materials is changing the ligand from O to the heavier chalcogenides S and Se, which can favor the formation of the O3-type structure. Colombet *et al.* reported crystalline  $\text{Na}_2\text{TiS}_3$  in 1978 while investigating the  $\text{Na}_2\text{S-TiS}_2$  system.<sup>10</sup> Based on visual inspection of the PXRD pattern, they speculated on structural similarity with  $\text{Na}_2\text{SnS}_3$ , implying a layered O3-type structure.<sup>11</sup> Pelé investigated  $\text{Na}_2\text{TiS}_3$  for the first time as a cathode material (theoretical capacity of 282 mAh/g), but problems with the electrolyte (1M  $\text{NaPF}_6$  in tetraethylene glycol dimethylether) prevented full exploitation of the theoretical capacity.<sup>12</sup> Following this lead, Nasu *et al.* described the synthesis and electrochemical cycling properties of three polymorphs of  $\text{Na}_2\text{TiS}_3$ : amorphous, cubic (disordered rock salt structure) and layered, which they targeted by applying different ball milling and heating procedures.<sup>13,14</sup> In all-solid-state cell configurations using glassy  $\text{Na}_3\text{PS}_4$  as a solid electrolyte and  $\text{Na}_{15}\text{Sn}_4$  as the anode, they achieved reversible capacities of 250 mAh/g (amorphous), 270 mAh/g (cubic) and 140 mAh/g (crystalline) in the voltage range of 0.8 V - 3.2 V.

Such high electrochemical activity in  $\text{Na}_2\text{TiS}_3$  is somewhat surprising bearing in mind that  $\text{Ti}^{4+}$  has a  $d^0$  electron configuration and that isostructural  $\text{Li}_2\text{TiS}_3$  is electrochemically inactive. Thus, the answer must lie with the contribution of the anion sublattice to the charge compensation, implying  $\text{S}^{2-/n}$ -anionic redox. Sulfide-based materials exhibit a large range of formal oxidation states, ranging from  $\text{S}^{2-}$  in  $\text{Li}_2\text{TiS}_3$ , to mixed  $\text{S}^{2-}/(\text{S}_2)^{2-}$  in  $\text{TiS}_3$ , to dimerized  $(\text{S}_2)^{2-}$  in  $\text{FeS}_2$  and finally to  $(\text{S}_2)^{1-}$  in  $\text{CuS}_2$ .<sup>15-19</sup> This versatile anion redox chemistry was already exploited in  $\text{Li}_2\text{TiS}_3$  by cation-doping (*e.g.*  $\text{Ti}^{3+}$ ,  $\text{Co}^{2+}$ ,  $\text{Fe}^{2+}$ )<sup>15,20,21</sup> or ball milling,<sup>22</sup> which both unlock dynamic anionic redox processes upon electrochemical cycling. Recently, we substituted  $\text{S}^{2-}$  for  $\text{Se}^{2-}$  along the full  $\text{Li}_2\text{TiS}_{3-x}\text{Se}_x$  solid solution and observed a bell shaped activation curve, *i.e.* the endmembers exhibit negligible activity while the mixed compounds show significant capacity. We proposed that introduction of Se breaks the local symmetry and leads to local distortions around the  $\text{TiCh}_6$  ( $\text{Ch} = \text{S}, \text{Se}$ ) octahedra, which activates anionic redox.<sup>23</sup> Intrigued by this novel approach to anionic redox in  $d^0$  TM based materials, we decided to revisit  $\text{Na}_2\text{TiS}_3$ , its structural homologues  $\text{Na}_2\text{TiSe}_3$ ,  $\text{Na}_2\text{ZrS}_3$ ,  $\text{Na}_2\text{ZrSe}_3$  and finally the mixed  $\text{Na}_{1.5}[\text{Li}_{0.5}\text{Ti}]\text{S}_3$  phase in an attempt to strengthen our understanding of anionic redox in sulfide based materials.

In a first step, we examined the synthetic conditions for crystalline  $\text{Na}_2\text{MCh}_3$  ( $\text{M} = \text{Ti}, \text{Zr}$ ;  $\text{Ch} = \text{S}, \text{Se}$ ). As reported, one can readily obtain a crystalline  $\text{Na}_2\text{TiS}_3$  phase by sintering the binaries  $\text{Na}_2\text{S}$  and  $\text{TiS}_2$  in evacuated quartz tubes at 773 K, while the firing conditions were optimized for the other compositions (see SI). Crystalline  $\text{Na}_2\text{TiS}_3$  demonstrates electron diffraction patterns (ED) characteristic of a layered O3-type structure (Figure 1a) manifested by the sharp brightest spots which can be indexed with the  $R\bar{3}m$  unit cell ( $a = 3.7 \text{ \AA}$ ,  $c = 19.7 \text{ \AA}$ ). EDX compositional maps (Figure S1) of the  $\text{Na}_2\text{TiS}_3$  sample indicate

homogeneous distribution of Na, Ti and S. Quantitative analysis gives a Na:Ti:S atomic ratio of 2.02(4):0.97(4):3.01(3), which is in good agreement with the nominal composition. Robust “honeycomb” ordering of the Na and Ti cations in the mixed  $[\text{Na}_{1/3}\text{Ti}_{2/3}]$  layers is indicated by extra spots and diffuse intensity lines along  $c^*$  clearly visible in the  $[-110]$  ED pattern. The interlayer ordering is however violated by numerous stacking faults visible in the  $[110]$  HAADF-STEM image (Figure 1b). The “honeycomb” superstructure can be more rigorously described by a monoclinic distortion of the rhombohedral cell. A combined SXRD/NPD<sup>24</sup> Rietveld refinement was carried out in the monoclinic space group  $C2/m$  (Figure S2, Table S1) which confirms that  $\text{Na}_2\text{TiS}_3$  adopts an O3-type structure, in which edge-sharing  $\text{MS}_6$  octahedra ( $M = \text{Na}, \text{Ti}$ ) form two types of layers:  $[\text{Na}]_2\text{S}_2$  layers and partially honeycomb ordered  $[\text{Na}_{1/3}\text{Ti}_{2/3}]\text{S}_2$  layers, which are stacked along the  $c$  axis. Minor traces of  $\text{TiO}_2$  (Anatase, Rutile) were detected in the SXRD pattern which originate from oxide impurities in the commercial  $\text{Na}_2\text{S}$  precursor. Rietveld refinements of the heavier homologues (Figure S3, S4, Table S2-S4), show that  $\text{Na}_2\text{TiSe}_3$ ,  $\text{Na}_2\text{ZrS}_3$  and  $\text{Na}_2\text{ZrSe}_3$  crystallize isostructurally to  $\text{Na}_2\text{TiS}_3$ , in accordance with what had already been reported for the zirconates.<sup>25,26</sup> In the case of  $\text{Na}_2\text{ZrS}_3$ , additional superstructure reflections associated with O6 stacking sequences are clearly visible (inset Figure S4a). The origin of these has already been thoroughly discussed for  $\text{Na}_3\text{Ni}_2\text{BiO}_6$ <sup>27</sup> and  $\text{Na}_{1.5}[\text{Li}_{0.5}\text{Ir}]\text{O}_3$ .<sup>8</sup>

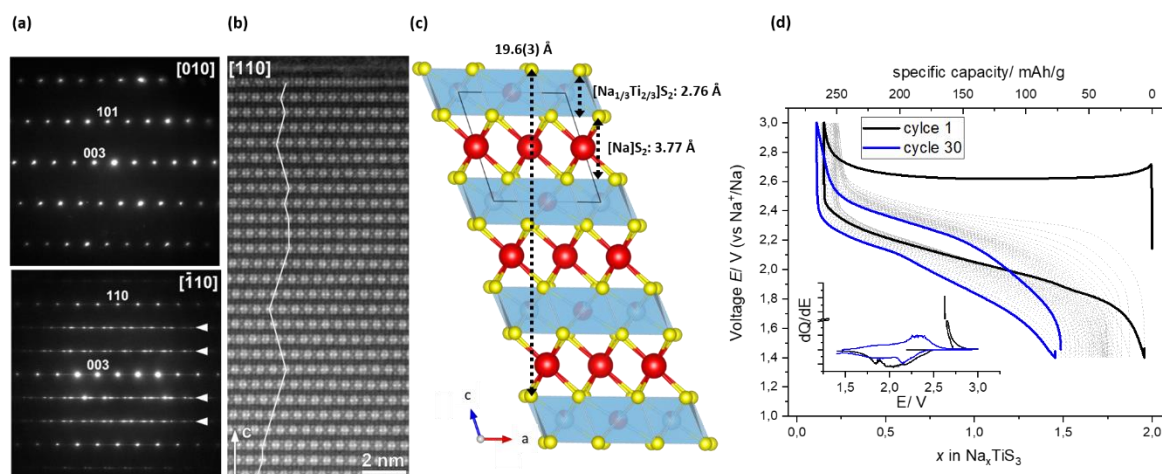


Figure 1: Structural and electrochemical characterization of  $\text{Na}_2\text{TiS}_3$  (a) ED patterns indexed with the  $R\bar{3}m$  space group, reflections and diffuse intensity due to the Na-Ti “honeycomb” ordering are marked with arrowheads. (b)  $[110]$  HAADF-STEM image, stacking faults along  $c$  are visible by random lateral displacements of the  $[\text{Na}_{1/3}\text{Ti}_{2/3}]\text{S}_2$  blocks traced with zig-zag line. (c) structural model as obtained from a combined SXRD-NPD Rietveld refinement viewed along the  $b$  axis, forming a layered O3-type structure. (d) Galvanostatic cycling of  $\text{Na}_2\text{TiS}_3$  vs  $\text{Na}^+/\text{Na}$ . Atoms and polyhedral are colored as follows - red: sodium; blue: titanium; sulfur: yellow.

In 2020 Saha proposed the use of 1 M  $\text{NaPF}_6$  in propylene carbonate (PC) as electrolyte in a  $\text{Na}_2\text{TiS}_3|\text{Na}$  electrochemical cell, which improved the reversibility of the cycling.<sup>28</sup> Galvanostatic experiments on  $\text{Na}_2\text{MCh}_3$  ( $M = \text{Ti}, \text{Zr}; \text{Ch} = \text{S}, \text{Se}$ ) vs  $\text{Na}^+/\text{Na}$  confirm the suitability of this electrolyte, as up to 1.8 Na can be extracted on oxidation from the titanates (Figure 1d). In the case of  $\text{Na}_2\text{TiS}_3$ , close inspection of the voltage trace reveals a bump at the onset of the initial oxidation, which is not present for  $\text{Na}_2\text{TiSe}_3$  (Figure S3b). This potential spike is followed by a plateau indicative of a biphasic process. On subsequent cycling, the voltage trace changes to an S-shape, symptomatic of the formation of solid-solutions between the charged and discharged states. The average voltage is lowered on going from the sulfide to the selenide which is a direct consequence from the lower electronegativity of Se compared to S, similar to observed in  $\text{Li}_2\text{TiS}_{3-x}\text{Se}_x$  or  $\text{Li}_2\text{FeS}_{2-x}\text{Se}_x$ .<sup>23,29</sup> Throughout cycling both materials are plagued by voltage hysteresis, but better orbital overlap in the selenides allows for a partial reduction of the voltage gap in  $\text{Na}_2\text{TiSe}_3$  to 240 mV compared to 500 mV in the  $\text{Na}_2\text{TiS}_3$ . This extremely high polarization can be lowered to 250 mV in a GITT experiment after a 4 h relaxation

period (Figure S5a). Upon 30 cycles the capacity drops drastically by 25 % and 65% in  $\text{Na}_2\text{TiS}_3$  and  $\text{Na}_2\text{TiSe}_3$ , respectively, coupled to significant voltage fade. To verify that the electrochemical capacity in  $\text{Na}_2\text{TiS}_3$  is not simply triggered by an off-stoichiometric pristine material (presence of  $\text{Ti}^{3+}$ ), we started electrochemical cells on discharge. However, the first discharge capacity is negligible (Figure S5b). Interestingly, opening the discharge voltage to 0.2 V does not lead to the reversible utilization of the  $\text{Ti}^{4+}/\text{Ti}^{3+}$  couple, which in  $\text{TiS}_2$  is responsible for the electrochemical activity. At the precise stoichiometry of  $\text{Na}_2\text{TiS}_3$ , all octahedral voids are occupied, leaving only tetrahedral interstices for hosting additional  $\text{Na}^+$  ions. Instead of intercalation, the voltage curve indicates conversion type reaction at low potentials leading to irreversible structural degradation (Figure S5c). Turning to the zirconates, these materials exhibit nearly no reversible capacity at all. Introduction of more electropositive Zr raises energy of the empty cationic d-bands and consequently increases the band gap, which is corroborated by a color change from black/grey ( $\text{Na}_2\text{TiS}_3$ ) to brown/orange ( $\text{Na}_2\text{ZrS}_3$ ). Eventually this increased band gap reduces electronic conductivity of  $\text{Na}_2\text{ZrS}_3$  and thus impedes bulk oxidation.

To gain more insight into this structural transformation, we carried out *operando* PXRD and *ex situ* SXR experiments on  $\text{Na}_2\text{TiS}_3$  and  $\text{Na}_2\text{TiSe}_3$  cycled vs  $\text{Na}^+/\text{Na}$ . In both materials, the first oxidation process is of biphasic nature: a broad reflection associated with the formation of a secondary  $\text{Na}_x\text{TiCh}_3$  phase grows gradually in intensity, while the pristine material is consumed (Figure 2a, Figure S3c). At full charge  $\text{Na}_x\text{TiCh}_3$  exhibits low crystallinity – only the 00 $l$  reflection, associated with the interlayer spacing is well defined ( $d=6\text{ \AA}$ ) (SXR pattern, Figure 2b), impeding meaningful structural refinement. Upon discharge a solid-solution is formed with concomitant increase of crystallinity. The discharged  $\text{Na}_2\text{TiS}_3$  material regains its O3-type structure, as determined by a Rietveld refinement on SXR data (Figure 2c,d; Table S5). However, the Na-Ti honeycomb ordering is lost and notable peak broadening coupled to increased isotropic atomic displacement parameters  $U_{\text{iso}}$  reflect a considerable degree of disorder. On consecutive cycling, a reversible solid-solution is formed along  $\text{Na}_2\text{TiCh}_3\text{-Na}_x\text{TiCh}_3$ . This response to oxidation contrasts starkly with  $\text{Li}_2\text{TiS}_3$ , which is electrochemically inactive and with the structural evolution of  $\text{Li}_2\text{TiS}_{2.4}\text{Se}_{0.6}$ , for which a monophasic response upon oxidation was witnessed.

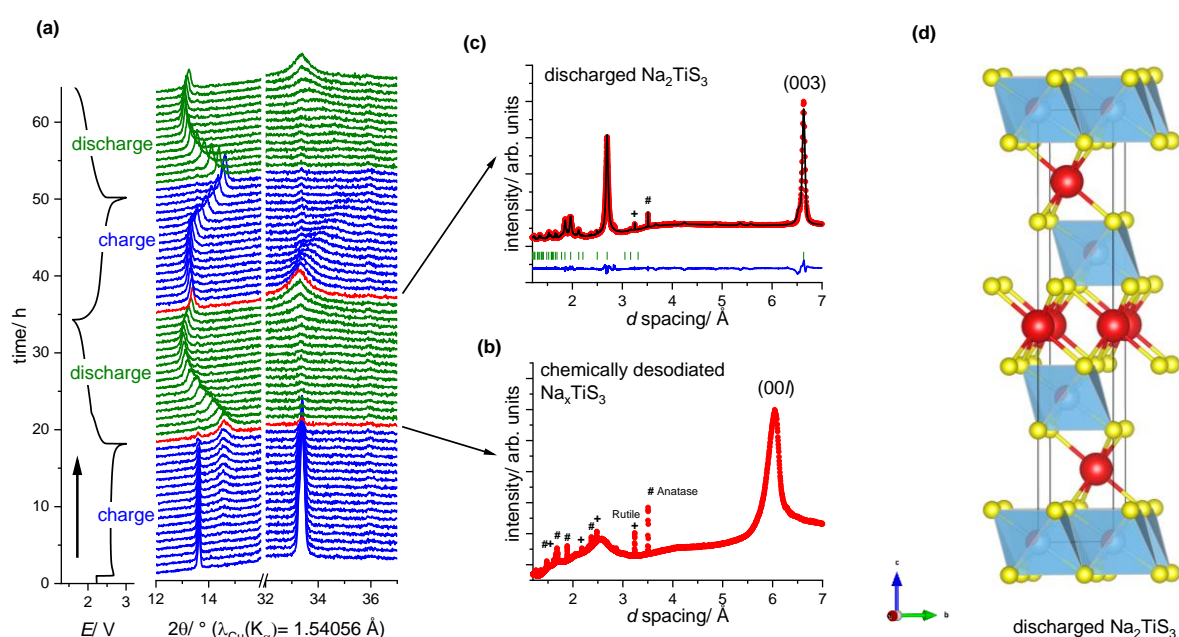


Figure 2: Structural evolution of  $\text{Na}_2\text{TiS}_3$  cycled against  $\text{Na}^+/\text{Na}$  (a) operando PXRD experiment on two electrochemical cycles (b) SXRD pattern of chemically charged  $\text{Na}_x\text{TiS}_3$ , the symbols '#' and '+' denote the position of the Bragg reflections of the electrochemically inactive  $\text{TiO}_2$  polymorphs Rutile and Anatase, already observed in the pristine material. The charged  $\text{Na}_x\text{TiS}_3$  material is manifested by a broad reflection at  $d=6 \text{ \AA}$ . (c) Rietveld refinement of discharged  $\text{Na}_2\text{TiS}_3$  based on SXRD data (d) Refined structural model of discharged  $\text{Na}_2\text{TiS}_3$ . Atoms and polyhedral are colored as follows - red: sodium; blue: titanium; sulfur: yellow.

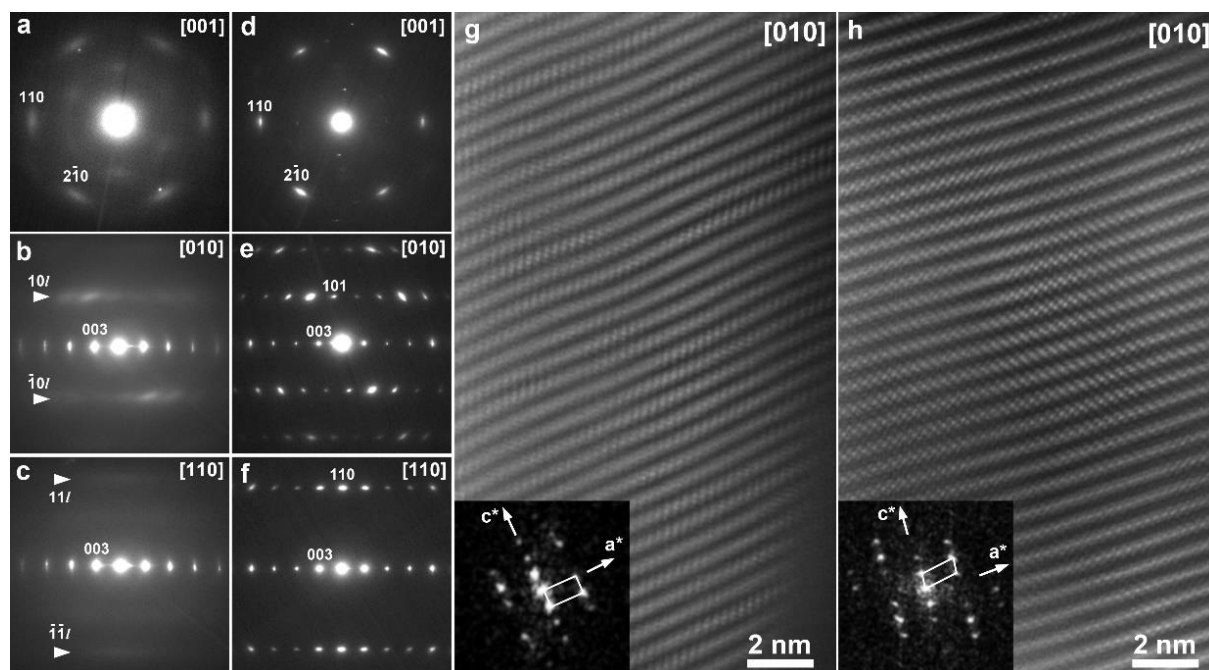


Figure 3: Structural evolution of  $\text{Na}_2\text{TiS}_3$  upon desodiation (a,b,c,g) and subsequent sodiation (d,e,f,h). The ED patterns are indexed with the  $R\bar{3}m$  space group. The  $h0l$  and  $hhl$  diffuse intensity lines in the ED patterns of the desodiated phase (a,b,c) are marked with arrowheads. Fourier transforms are shown as insets in the HAADF-STEM images of the desodiated (g) and sodiated (h) phases; the reciprocal lattice mesh is outlined in the Fourier transforms.

The structure changes upon desodiation and sodiation of  $\text{Na}_2\text{TiS}_3$  were finally assessed with transmission electron microscopy. The ED patterns of the desodiated phase (Figure 3a,b,c) demonstrate only the  $00l$  reflections which remain relatively sharp whereas all other reflections are substituted with poorly structured diffuse intensity manifesting itself as elongated blobs in the  $[001]$  ED pattern and as broad lines of modulated intensity in the  $[010]$  and  $[110]$  ED patterns. This picture is very typical for the layered systems with 2D disorder in which the layers remain regularly spaced causing sharp  $00l$  reflections whereas the atomic positions within the layers and between the layers lose coherency. In fact, elongation of the  $00l$  reflections in the direction perpendicular to  $c^*$  (Figure 3b,c) also indicates that the layers demonstrate small local variation of orientation (*i.e.* become wavy). These features are supported by  $[010]$  HAADF-STEM image (Figure 3g) which shows that the layers contain ordered and disordered areas. The latter are visible by absence of clear dot pattern which becomes smeared due to loss of electron channeling conditions caused by random atomic displacements. Fourier transform from the locally ordered area indicates changing of the layer stacking mode from O3 to O1 (seen by a rectangular reciprocal lattice mesh outlined in the Fourier transform (insert in Figure 3g)). Local disorder and gliding of the layers introduce strong strain causing wave-like deformation of the layers, also easily discernible from Figure 3g. Upon sodiation the atomic order within the layers is largely restored as is evident from sharpening of the reflections in the ED patterns (Figure 3d,e,f) and clear pattern of atomic columns in the  $[010]$  HAADF-STEM image (Figure 3h). The  $[010]$  ED pattern (Figure 3e) and Fourier transform of the HAADF-STEM image (see the oblique reciprocal lattice mesh in the insert in Figure 3h) show that the O3 stacking is fully recovered. Absence of “honeycomb” reflections (compare the  $[-110]$  ED patterns in Figure 1a and Figure 3f) witnesses

complete suppression of the Na-Ti intralayer ordering. Shuffling the Ti atoms upon suppression of the “honeycomb” ordering might be at the origin of strong local atomic disorder observed in the desodiated phase.

Motivated by these results we assembled  $\text{Na}_2\text{TiS}_3|\text{Li}$  cells (electrolyte: LP30). Interestingly, these cells show very similar electrochemical behavior, even though we evidence a significantly smaller polarization (Figure S6) compared to cycling vs Na. The voltage gap is reduced to 350 mV at C/10 rate and can be mitigated to 170 mV in a GITT experiment after 4 h relaxation. *Operando* PXRD experiments in the  $\text{Na}_2\text{TiS}_3|\text{Li}$  configuration show that the material follows the same structural path as when cycled vs Na, in particular forming a very disordered  $A_x\text{TiS}_3$  ( $A = \text{Li}, \text{Na}; x < 0.3$ ) framework at the end of charge. Already in the 1980’s, crystalline  $\text{TiS}_3$  (obtained by calcination of Ti and S at 773 K) was identified as a potential high-energy cathode material due to its large theoretical capacity. Up to three Li ions can be inserted utilizing both the anionic  $(\text{S}_2)^{2-}/\text{S}^{2-}$  and cationic  $\text{Ti}^{4+}/\text{Ti}^{3+}$  redox couples. But at that time the application of  $\text{TiS}_3$  was hampered by limited reversibility and voltage fade.<sup>30–34</sup> Intrigued, we directly synthesized electrochemically active  $A_x\text{TiS}_3$  via two routes: (a) electrochemical desodiation of  $\text{Na}_2\text{TiS}_3$  (b) chemical desodiation of  $\text{Na}_2\text{TiS}_3$  using  $\text{I}_2$  in acetonitrile. Both materials demonstrate reversible discharge capacities ( $>275 \text{ mAh/g}$ ) and high energy densities ( $> 600 \text{ Wh/kg}$ ) when cycled against a Li anode (Figure 4).

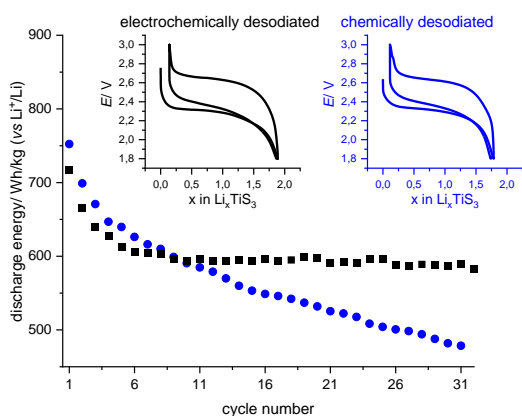


Figure 4: Electrochemical behavior of desodiated  $\text{Na}_x\text{TiS}_3$  ( $x < 0.3$ ) cycled against a Li metal anode.

In  $\text{Li}_2\text{TiS}_{3-x}\text{Se}_x$ , we previously identified local distortions of the heteroleptic  $\text{TiCh}_6$  octahedra as the key to unlock anionic redox.<sup>23</sup> In order to get a grasp on local distortion in  $\text{Na}_2\text{TiS}_3$  compared to  $\text{Li}_2\text{TiS}_3$ , EPR experiments were run at ambient temperature, 110 K and 5 K (Figure 5a, Figure S7). While the spectra for  $\text{Li}_2\text{TiS}_3$  are featureless at ambient temperature except for a signal of a non-localized electron ( $g = 2.0024$ ), we notice a more complicated spectrum for  $\text{Na}_2\text{TiS}_3$ . In addition to a signal of the free electron, we observe an anisotropic  $\text{Ti}^{3+}$  environment with three distinct  $g$  values ( $g_x = 1.985$ ,  $g_y = 1.962$ ,  $g_z = 1.946$ ). The onset of a  $\text{Ti}^{3+}$  signal, not expected at first in  $\text{Na}_2\text{Ti}^{4+}\text{S}_3$ , was previously explained for  $\text{Li}_2\text{TiS}_{3-x}\text{Se}_x$  from an internal ligand-to-metal charge transfer by temperature-driven electron localization.<sup>23</sup> With decreasing temperature, one can follow increased distortion of the octahedral symmetry with finally a fully localized electron on the Ti orbital at 5 K in both compounds (Figure 5b). While in  $\text{Li}_2\text{TiS}_3$  dipolar interactions between Li and Ti dominate, echo detection mode uncovers superhyperfine coupling in  $\text{Na}_2\text{TiS}_3$ . The pseudo modulation of the spectrum (inset) shows two sets of 7 lines for the two eigenvalues ( $g_x$ ,  $g_y$ ) of the  $\text{Ti}^{3+}$  tensor. These lines can be attributed to Fermi contact coupling of  $\text{Ti}^{3+}$  with two equivalent sodium nuclei ( $I = 3/2$ ). Thus, the temperature dependent distortion of the  $\text{TiS}_6$  octahedra is accompanied by a shortening of the Na-Ti distance.

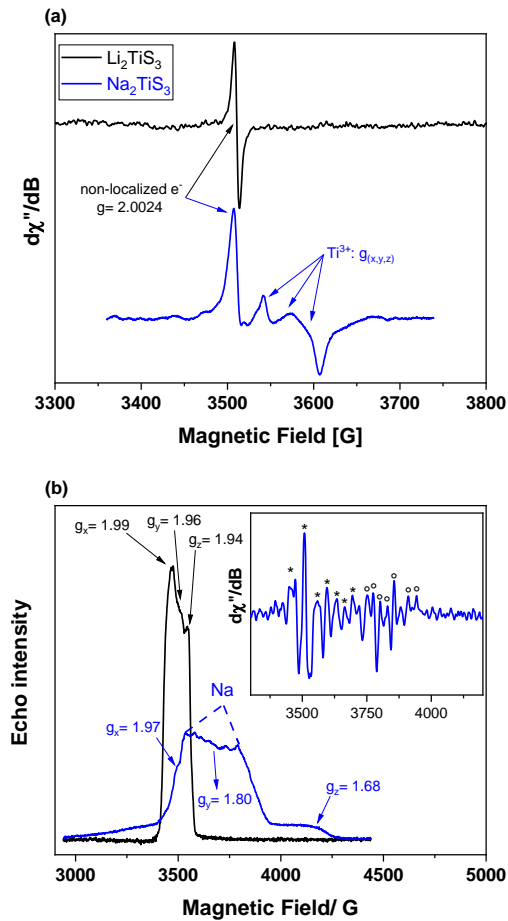


Figure 5: EPR spectra of  $\text{Li}_2\text{TiS}_3$  (black) and  $\text{Na}_2\text{TiS}_3$  (blue) at (a) ambient temperature and (b) at 5 K. The inset shows the superhyperfine coupling between  $g_x$  and  $g_y$  of the anisotropic  $\text{Ti}^{3+}$  with two equivalent Na atoms (nuclear spin  $I=3/2$ ), which results in  $2nI+1$  lines per coupling (in total  $2 \times 7$  lines).

Analysis of interatomic distances and bond lengths of the crystallographic models obtained by Rietveld refinement show that the “cubic” close-packed anion sublattice is significantly distorted in  $\text{Na}_2\text{TiS}_3$  compared to  $\text{Li}_2\text{TiS}_3$ . By comparing the 12 closest S-S contacts for the crystallographically distinct S1 and S2 atoms in both materials, we clearly see a wider spread of the distances in  $\text{Na}_2\text{TiS}_3$  (3.2 Å - 4.5 Å) in contrast to  $\text{Li}_2\text{TiS}_3$  (3.3 Å - 3.9 Å) (Figure 6a). This is equivalently expressed by more irregular bond lengths in the  $\text{MS}_6$  octahedra ( $M = \text{Li, Na, Ti}$ ) (Figure 6b). Interestingly, the Ti1-S and Ti2-S bond lengths are very uniform (Figure 6c). Similarly, we cannot identify a significant difference in distortion of the  $\text{AS}_6$  octahedra between  $\text{Na}_2\text{TiS}_3$  and  $\text{Li}_2\text{TiS}_3$  (Figure 6d). In conclusion, we state that the  $\text{MS}_6$  metal octahedra are not significantly distorted, but that a distortion of the anion sublattice in  $\text{Na}_2\text{TiS}_3$  is caused by the significantly longer intralayer distance in the  $[\text{Na}]_2\text{S}_2$  slab (3.77 Å) compared to the mixed  $[\text{Na}_{1/3}\text{Ti}_{2/3}]_2\text{S}_2$  slab (2.76 Å) (see Figure 1), which are more even in  $\text{Li}_2\text{TiS}_3$ . A similar conclusion can be reached when analyzing the crystallographic model of  $\text{Na}_2\text{TiSe}_3$  (Figure S8).



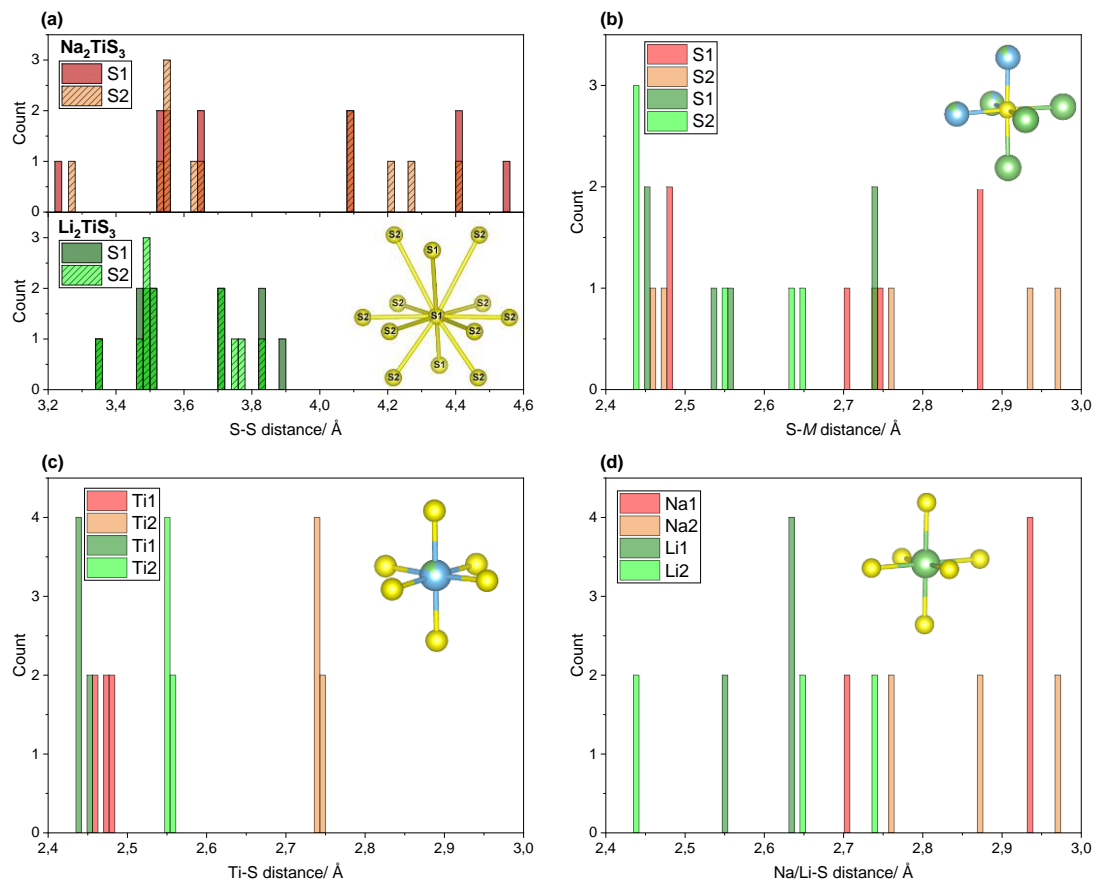


Figure 6: Analysis of atomic distances in  $\text{Na}_2\text{TiS}_3$  and in  $\text{Li}_2\text{TiS}_3$  based on the crystallographic models. (a) distance between a given sulphur atom (S1 or S2) in the cubic close packed anion sublattice and its 12 nearest neighbors respectively. (b) bond lengths in a given  $\text{SM}_6$  octahedron. (c) bond lengths in a given  $\text{TiS}_6$  octahedron. (d) bond lengths in a given  $\text{AS}_6$  octahedron (A=Li, Na). Color code: red:  $\text{Na}_2\text{TiS}_3$ , green:  $\text{Li}_2\text{TiS}_3$ . Atoms are colored as follows - sulfur: yellow; blue : titanium; green: Li/Na.

## $\text{Na}_{1.5}[\text{Li}_{0.5}\text{Ti}]\text{S}_3$

To complete the investigation of this interesting class of materials, we explore the mixed alkaline  $\text{Na}_2\text{TiS}_3$ - $\text{Li}_2\text{TiS}_3$  ( $=\text{Na}_{2-x}\text{Li}_x\text{TiS}_3$ ) tie-line. The PXRD patterns of the  $x=0, 0.5, 1.0, 1.5, 2$  samples synthesized at 773 K are shown in Figure 7.

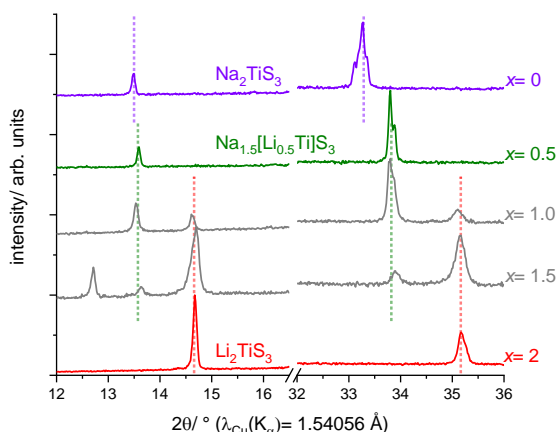


Figure 7: PXRD patterns of the reaction products obtained during the synthesis of the  $\text{Na}_{2-x}\text{Li}_x\text{TiS}_3$  compositions. The vertical lines indicate the position of the expected Bragg reflections for  $\text{Li}_2\text{TiS}_3$  (red),  $\text{Na}_2\text{TiS}_3$  (purple) and the new  $\text{Na}_{1.5}[\text{Li}_{0.5}\text{Ti}]\text{S}_3$  phase (green).

Alike for the  $\text{Na}_{2-x}\text{Li}_x\text{MnO}_3$ , we do not observe the formation of a solid solution, as for  $x = 1.5$  and  $x = 1.0$  multiple phases form. However, the composition of  $x = 0.5$  ( $\text{Na}_{1.5}\text{Li}_{0.5}\text{TiS}_3$ ) yields a single-phase PXRD pattern reminiscent of an O3-type structure. EDX analysis of the as-synthesized  $\text{Na}_{1.5}\text{Li}_{0.5}\text{TiS}_3$  gives a Na:Ti:S ratio of 1.48(7):1.04(5):3.00(4) for the main phase, which corresponds nicely with the nominal composition. Given that  $\text{Na}_{1.5}\text{Li}_{0.5}\text{TiS}_3$  is a stoichiometry-precise compound, we investigated the alkaline cation distribution among the layers by combined Rietveld refinement using NPD and SXRD data and TEM experiments. The best Rietveld fit could be obtained by entirely segregating Li and Na resulting in fully occupied  $[\text{Na}]\text{S}_2$  and honeycomb ordered  $[\text{Li}_{1/3}\text{Ti}_{2/3}]\text{S}_2$  layers with negligible degree of alkaline metal intermixing (Figure S9, S10, Table S6). Comparing the intensity profiles along the cationic columns in the [010] and [110] HAADF-STEM images of  $\text{Na}_{1.5}\text{Li}_{0.5}\text{TiS}_3$  and  $\text{Na}_2\text{TiS}_3$  confirms this assumption: virtually no intensity is detected at the Li sites of the  $[\text{Li}_{1/3}\text{Ti}_{2/3}]\text{S}_2$  layers, whereas noticeable intensity is seen at the Na sites in  $[\text{Na}_{1/3}\text{Ti}_{2/3}]\text{S}_2$  (Figure S11, S12). Both SXRD and TEM experiments reveal the presence of trace amounts of titanium dioxide (Anatase, Rutile),  $\text{Na}_2\text{TiS}_3$  and  $\text{Na}_5\text{Li}_3\text{Ti}_2\text{S}_8$  (compare to Table S7).<sup>35</sup>

The exchange of Na for Li in  $\text{Na}_2\text{TiS}_3$  has a notable impact on the electrochemical behavior: while from  $\text{Na}_2\text{TiS}_3$  up to 1.8 alkaline cations can be extracted upon oxidation, we succeed on the removal of solely 1.5 alkaline cations from  $\text{Na}_{1.5}[\text{Li}_{0.5}\text{Ti}]\text{S}_3$  (regardless of whether cycled vs  $\text{Na}^+/\text{Na}$  or  $\text{Li}^+/\text{Li}$ ) (Figure S13). This threshold links well the stoichiometry with the layered structure motif. Thus, we speculate that upon oxidation predominantly Na atoms are removed from the material, while the Li atoms remain inert – similar to observed in  $\text{Na}_1[\text{Li}_{1/3}\text{Mn}_{2/3}]\text{O}_2$  and  $\text{Na}_{0.75}[\text{Li}_{0.25}\text{Mn}_{0.75}]\text{O}_2$ .<sup>9,36</sup> Furthermore, the voltage traces differ significantly when cycled against sodium or lithium anodes: an increased polarization persists during subsequent cycles when cycled vs  $\text{Na}^+/\text{Na}$ , while the cycling vs  $\text{Li}^+/\text{Li}$  mirrors the behavior of  $\text{Na}_2\text{TiS}_3$ . GITT experiments during the 2<sup>nd</sup> electrochemical cycle reveal that this hysteresis is attributed to kinetic effects, as the relaxed voltage traces of  $\text{Na}_{1.5}[\text{Li}_{0.5}\text{Ti}]\text{S}_3$  cycled vs  $\text{Na}^+/\text{Na}$  or  $\text{Li}^+/\text{Li}$  match closely. Interestingly the average discharge voltage of  $\text{Na}_2\text{TiS}_3$  and  $\text{Na}_{1.5}[\text{Li}_{0.5}\text{Ti}]\text{S}_3$  cycled against  $\text{Li}^+/\text{Li}$  are very close. Lastly, *operando* PXRD experiments of cells cycled against  $\text{Na}^+/\text{Na}$  and  $\text{Li}^+/\text{Li}$  reveal that  $\text{Na}_{1.5}[\text{Li}_{0.5}\text{Ti}]\text{S}_3$  undergoes the same structural process upon electrochemical cycling as  $\text{Na}_2\text{TiS}_3$ .

Finally, an NMR study was carried out on  $\text{Na}_2\text{TiS}_3$  and  $\text{Na}_{1.5}[\text{Li}_{0.5}\text{Ti}]\text{S}_3$  at different states of charge, as this technique allows for the study of the local order in low-crystalline materials and the quantification of the Li and Na content. Figure 8 shows the experimental and predicted <sup>23</sup>Na and <sup>7</sup>Li spectra of  $\text{Na}_2\text{TiS}_3$  and  $\text{Na}_{1.5}[\text{Li}_{0.5}\text{Ti}]\text{S}_3$  at different states of charge.

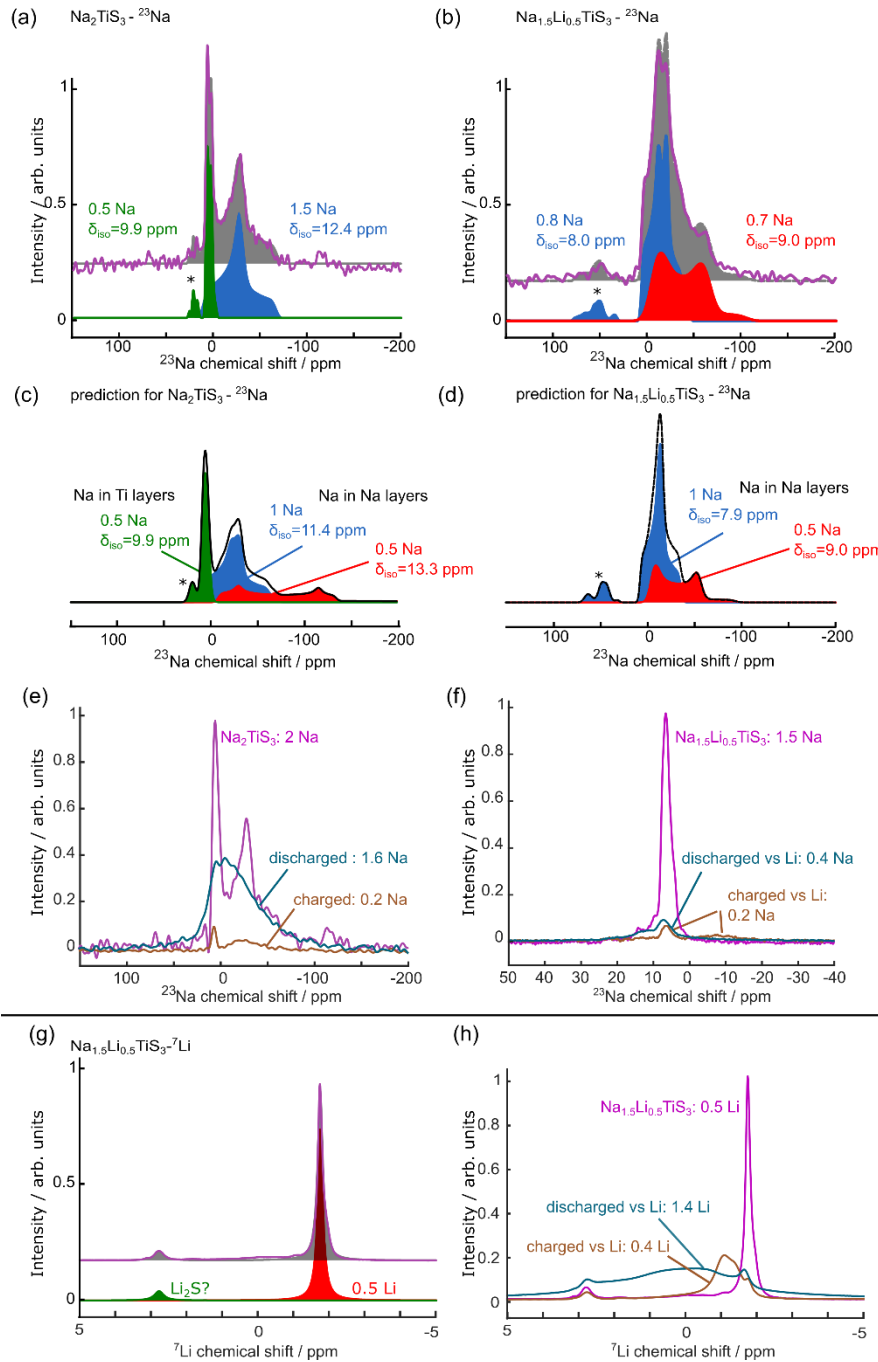


Figure 8:  $^{23}\text{Na}$  solid-state NMR spectra and fits of (a)  $\text{Na}_2\text{TiS}_3$  and (b)  $\text{Na}_{1.5}\text{Li}_{0.5}\text{TiS}_3$ . The Na content is obtained by the integration of the components of the fit. The asterisk indicates the band  $n=0$  of the satellite transition. (c, d) Predicted  $^{23}\text{Na}$  spectra based on the crystallographic models. (e, f) Quantitative analysis of the  $^{23}\text{Na}$  NMR spectra upon charge and discharge. (g) Experimental  $^7\text{Li}$  NMR spectrum and fit of  $\text{Na}_{1.5}\text{Li}_{0.5}\text{TiS}_3$ . An impurity phase is detected at 2.8 ppm which might relate to  $\text{Li}_2\text{S}$ . (h) Quantitative analysis of the  $^7\text{Li}$  NMR spectra upon charge and discharge vs  $\text{Li}^+/\text{Li}$ .

The  $^{23}\text{Na}$  NMR spectrum for  $\text{Na}_2\text{TiS}_3$  (Figure 8a) reveals a broad signal accounting for 1.5 Na (blue) and a sharper signal corresponding to 0.5 Na (green), which we relate to the different Na environments in the  $[\text{Na}]\text{S}_2$  and the mixed  $[\text{Na}_{1/3}\text{Ti}_{2/3}]\text{S}_2$  layers respectively. The complex shapes of the signals are due to the quadrupolar nature of the Na atomic spins (see SI, Tables S8-S11). In contrast the  $^{23}\text{Na}$  NMR spectrum of  $\text{Na}_{1.5}\text{Li}_{0.5}\text{TiS}_3$  (Figure 8b) is characterized by two broad signals accounting for 0.8 and 0.7 Na, indicative of non-symmetric environments. In order to confirm the negligible cation interlayer mixing, we performed planewave GIPAW predictions of the shifts based on the crystal structures. This approach was validated for  $\text{Na}_2\text{TiS}_3$  (Figure 8c): the assignment is confirmed with a sharp (green) signal

for Na in  $[\text{Na}_{1/3}\text{Ti}_{2/3}]\text{S}_2$  layers and two broad signals (blue and red) for Na in the  $[\text{Na}]\text{S}_2$  layer. Na mobility in that  $[\text{Na}]\text{S}_2$  layer results in the average signal detected experimentally. We then calculated the shifts for the mixed compound  $\text{Na}_{1.5}[\text{Li}_{0.5}\text{Ti}]\text{S}_3$  for the structure containing negligible cation interlayer mixing and obtained a good agreement (Figure 8d). When charged, the  $^{23}\text{Na}$  signal almost completely disappears for both materials, while the  $^7\text{Li}$  signal of the mixed phase is only slightly lowered. The charged samples have nominal compositions of  $\text{Na}_{0.2}\text{TiS}_3$  (Figure 8e) and  $\text{Na}_{0.2}[\text{Li}_{0.4}\text{Ti}]\text{S}_3$  respectively (Figure 8f,h). The significant broadening of the  $^7\text{Li}$  peak could be due to disorder induced by the amorphisation and/or Li migration, but we clearly observe a preferred removal of Na compared to Li. Upon discharge, a broad  $^{23}\text{Na}$  signal reappears for  $\text{Na}_2\text{TiS}_3$  indicating the reinsertion of 1.4 Na. Discharge against  $\text{Li}^+/\text{Li}$  results in preferential Li insertion with the resulting composition  $\text{Na}_{0.4}\text{Li}_{1.4}\text{TiS}_3$ . Quantitative analysis of the Na and Li content in the material confirms a combined alkaline metal content of  $\text{A}_{1.9}\text{TiS}_3$  as obtained from coulombic titration.

## Discussion/conclusion

The layered  $\text{A}_2\text{TiCh}_3$  family proves to be a versatile framework for fine-tuning structural and electrochemical properties. By moving from  $\text{Li}_2\text{TiS}_3$  to  $\text{Na}_2\text{TiS}_3$  and finally to  $\text{Na}_2\text{TiSe}_3$ , we detect reversible electrochemical activity in the  $\text{TiCh}_3$  framework. Desodiation of  $\text{Na}_2\text{TiS}_3$  yields a metastable  $\text{Na}_x\text{TiS}_3$  polymorph, which shows high discharge energy when cycled against a Li electrode (600 Wh/kg). Due to the  $d^0$  electron configuration in  $\text{Ti}^{4+}$  we associate this capacity to redox processes on the anion framework, although the underlying mechanisms have not been fully understood so far. Preliminary DFT calculations show that the band gap in  $\text{Na}_2\text{TiS}_3$  is larger than in  $\text{Li}_2\text{TiS}_3$ , thus ruling out that increased electronic conductivity is responsible for electrochemical activation in  $\text{Na}_2\text{TiS}_3$ . Analysis of EPR spectra and the crystallographic models indicate increased distortion of the S sublattice in  $\text{Na}_2\text{TiS}_3$  compared to  $\text{Li}_2\text{TiS}_3$ . However, these observations must be more rigorously tied to the emergence of electrochemical activity in  $\text{A}_2\text{TiCh}_3$  phases and consequently put into context of structural prerequisites for anionic redox. An in-depth computational paper dedicated to the charge compensation mechanisms in this family of materials is in preparation. Nevertheless, another explanation could lie in the energetics of the reaction pathway of the alkaline metal-driven electrochemical transformation from the pristine  $\text{A}_2\text{TiS}_3$  to the activated  $\text{TiS}_3$  framework. Introduction of more polarizable Se or Na might induce lattice softening and result in increased structural flexibility of the  $\text{TiCh}_3$  framework. Consequently, structural transformations in  $\text{Na}_2\text{TiS}_3$  (O3 – O1) or  $\text{Li}_2\text{TiS}_{3-x}\text{Se}_x$  (O3 – O3) might be possible due to lower kinetic barriers, while being impeded in  $\text{Li}_2\text{TiS}_3$ .

Along the  $\text{Li}_2\text{TiS}_3$ - $\text{Na}_2\text{TiS}_3$  tie-line we find only one stable compound, O3-type  $\text{Na}_{1.5}[\text{Li}_{0.5}\text{Ti}]\text{S}_3$ . NMR studies at different states of charge reveal that Na is preferentially removed from  $\text{Na}_{1.5}[\text{Li}_{0.5}\text{Ti}]\text{S}_3$ . As already observed in  $\text{Na}_{1.5}[\text{Li}_{0.5}\text{M}]\text{O}_3$  ( $M = \text{Mn, Ru}$ ), the precise Na:Li ratio is governed by the formation of distinct  $[\text{Na}]\text{S}_2$  and mixed  $[\text{Li}_{1/3}\text{Ti}_{2/3}]\text{S}_2$  layers. We finally test this rationale of mixing alkaline metals to stabilize the O3 structure motif by applying it to the  $\text{A}_2\text{TiO}_3$  ( $A = \text{Li, Na}$ ) system. In contrast to O3-type  $\text{Li}_2\text{TiO}_3$ ,<sup>37</sup>  $\text{Na}_2\text{TiO}_3$  is known to crystallize in three different non-layered polymorphs.<sup>38</sup> We hypothesize that mixing of Na and Ti in hypothetical  $[\text{Na}_{1/3}\text{Ti}_{2/3}]\text{O}_3$  layers incurs an energetic penalty but that this could be alleviated by synthesizing a mixed  $\text{Na}_{1.5}[\text{Li}_{0.5}\text{Ti}]\text{O}_3$  compound.  $\text{Na}_{1.5}[\text{Li}_{0.5}\text{Ti}]\text{O}_3$  was consequently targeted by calcination of  $\text{Na}_2\text{CO}_3$ ,  $\text{Li}_2\text{CO}_3$  and  $\text{TiO}_2$  (Anatase) at 923 K for 12 h. Indeed, analysis of the reaction product reveals the formation of an O3-type structure, as the main reflections of the PXRD pattern can be indexed to the rhombohedral  $R\bar{3}m$  space group ( $a = 3.00201(7)$  Å,  $c = 16.0751(6)$  Å) (Figure S14). Additional superstructure reflections and a  $\text{Li}_2\text{TiO}_3$  impurity are present at  $4 \text{ \AA} < d < 5 \text{ \AA}$ . Upon oxidation the material exhibits a short plateau at 4.6V vs  $\text{Li}^+/\text{Li}$  in the first cycle at which  $\sim 0.3$  A can be removed. However, almost no capacity is recovered on discharge. In transition metal oxides,

such an irreversible oxidation process ('activation plateau') is commonly associated to oxygen evolution.

We conclude that the layered transition metal chalcogenides ( $A_2TiCh$ ) constitute an exciting and challenging field for solid-state chemists in the search for new materials. The compositional diversity enables rational tailoring of electrochemical properties while allowing for the study of elusive phenomena such as anionic redox. We presented a strategy to unlock the electrochemical activity in the  $TiS_3$  framework, nurturing the long sought after dream of developing high-energy cathode materials devoid of expensive, rare or toxic transition metals.

#### **Acknowledgements:**

The authors thank M.-L. Doublet and C. Robert for DFT band gap calculations and D. Massiot, and F. Fayon for insightful discussions on NMR. The authors warmly acknowledge E. Suard and M. Avdeev for performing NPD diffraction experiments on the D2B beamline at ILL (Institute Laue-Langevin, Grenoble, France) and on the Echidna diffractometer, ANSTO (Australian Nuclear Science and Technology Organisation) respectively. A.M.A. thanks AICF of Skoltech for providing access to transmission electron microscopy equipment. J.-M.T. and B.L acknowledge funding from the European Research Council (ERC) (FP/2014)/ERC Grant-Project 670116-ARPEMA. This work used the 11-BM mail service of the Advanced Photon Source, a US Department of Energy (DOE) Office of Science User Facility operated for the DOE Office of Science by Argonne National Laboratory under contract no. DE-AC02-06CH11357. Financial support from the IR-RMN-THC Fr3050 CNRS for conducting the research is gratefully acknowledged.

- (1) Delmas, C.; Fouassier, C.; Hagenmuller, P. Structural Classification and Properties of the Layered Oxides. *Phys. B+C* **1980**, *99* (1), 81–85. [https://doi.org/https://doi.org/10.1016/0378-4363\(80\)90214-4](https://doi.org/https://doi.org/10.1016/0378-4363(80)90214-4).
- (2) McCalla, E.; Abakumov, A. M.; Saubanère, M.; Foix, D.; Berg, E. J.; Rousse, G.; Doublet, M.-L.; Gonbeau, D.; Novák, P.; Van Tendeloo, G.; Dominko, R.; Tarascon, J.-M. Visualization of O-O Peroxo-like Dimers in High-Capacity Layered Oxides for Li-Ion Batteries. *Science* (80-. ). **2015**, *350* (6267), 1516 LP – 1521. <https://doi.org/10.1126/science.aac8260>.
- (3) Sathiya, M.; Abakumov, A. M.; Foix, D.; Rousse, G.; Ramesha, K.; Saubanère, M.; Doublet, M. L.; Vezin, H.; Laisa, C. P.; Prakash, A. S.; Gonbeau, D.; VanTendeloo, G.; Tarascon, J.-M. Origin of Voltage Decay in High-Capacity Layered Oxide Electrodes. *Nat. Mater.* **2015**, *14* (2), 230–238. <https://doi.org/10.1038/nmat4137>.
- (4) Strobel, P.; Lambert-Andron, B. Crystallographic and Magnetic Structure of Li<sub>2</sub>MnO<sub>3</sub>. *J. Solid State Chem.* **1988**, *75* (1), 90–98. [https://doi.org/https://doi.org/10.1016/0022-4596\(88\)90305-2](https://doi.org/https://doi.org/10.1016/0022-4596(88)90305-2).
- (5) Mogare, K. M.; Friese, K.; Klein, W.; Jansen, M. Syntheses and Crystal Structures of Two Sodium Ruthenates: Na<sub>2</sub>RuO<sub>4</sub> and Na<sub>2</sub>RuO<sub>3</sub>. *Zeitschrift für Anorg. und Allg. Chemie* **2004**, *630* (4), 547–552. <https://doi.org/https://doi.org/10.1002/zaac.200400012>.
- (6) Bastow, T. J.; Hobday, M. E.; Smith, M. E.; Whitfield, H. J. Structural Characterisation of Na<sub>2</sub>ZrO<sub>3</sub>. *Solid State Nucl. Magn. Reson.* **1994**, *3* (2), 49–57. [https://doi.org/https://doi.org/10.1016/0926-2040\(94\)90023-X](https://doi.org/https://doi.org/10.1016/0926-2040(94)90023-X).
- (7) Ye, F.; Chi, S.; Cao, H.; Chakoumakos, B. C.; Fernandez-Baca, J. A.; Custelcean, R.; Qi, T. F.; Korneta, O. B.; Cao, G. Direct Evidence of a Zigzag Spin-Chain Structure in the Honeycomb Lattice: A Neutron and x-Ray Diffraction Investigation of Single-Crystal Na<sub>2</sub>IrO<sub>3</sub>. *Phys. Rev. B* **2012**, *85* (18), 180403.
- (8) Perez, A. J.; Rousse, G.; Tarascon, J.-M. Structural Instability Driven by Li/Na Competition in Na(Li<sub>1/3</sub>Ir<sub>2/3</sub>)O<sub>2</sub> Cathode Material for Li-Ion and Na-Ion Batteries. *Inorg. Chem.* **2019**, *58* (22), 15644–15651. <https://doi.org/10.1021/acs.inorgchem.9b02722>.
- (9) Wang, Q.; Mariyappan, S.; Rousse, G.; Morozov, A. V; Porcheron, B.; Dedryvère, R.; Wu, J.; Yang, W.; Zhang, L.; Chakir, M.; Avdeev, M.; Deschamps, M.; Yu, Y.-S.; Cabana, J.; Doublet, M.-L.; Abakumov, A. M.; Tarascon, J.-M. Unlocking Anionic Redox Activity in O3-Type Sodium 3d Layered Oxides via Li Substitution. *Nat. Mater.* **2021**, *20* (3), 353–361. <https://doi.org/10.1038/s41563-020-00870-8>.
- (10) Colombet, P.; Danot, M.; Jumas, J.-C.; Philippot, E. Sur Les Systèmes TiS<sub>2</sub> - A<sub>2</sub>S (A= Na et K). *Comptes rendus Hebd. des séances l'Académie des Sci. Série C, Sci. Chim.* **1978**, *287*, 411.
- (11) Mark, W.; Lindqvist, O.; Jumas, J.-C.; Philippot, E. The OD Structure of Na<sub>2</sub>SnS<sub>3</sub>. Determination and Refinement of an MDO Structure. *Acta Crystallogr. Sect. B* **1974**, *30* (11), 2620–2628.
- (12) Pelé, V. Nouveaux Matériaux d'électrodes Pour Microbatteries Au Sodium, Université de Bordeaux, 2016.
- (13) Nasu, A.; Otoyama, M.; Sakuda, A.; Hayashi, A.; Tatsumisago, M. Amorphous Na<sub>2</sub>TiS<sub>3</sub> as an Active Material for All-Solid-State Sodium Batteries. *Chem. Lett.* **2019**, *48* (3), 288–290. <https://doi.org/10.1246/cl.180895>.
- (14) Nasu, A.; Otoyama, M.; Sakuda, A.; Hayashi, A.; Tatsumisago, M. Mechanochemical Synthesis of Cubic Rocksalt Na<sub>2</sub>TiS<sub>3</sub> as Novel Active Materials for All-Solid-State Sodium Secondary Batteries. *J. Ceram. Soc. Japan* **2019**, *127* (8), 514–517. <https://doi.org/10.2109/jcersj2.19086>.

- (15) Flamary-Mespoulie, F.; Boulineau, A.; Martinez, H.; Suchomel, M. R.; Delmas, C.; Pecquenard, B.; Le Cras, F. Lithium-Rich Layered Titanium Sulfides: Cobalt- and Nickel-Free High Capacity Cathode Materials for Lithium-Ion Batteries. *Energy Storage Mater.* **2020**, *26*, 213–222. <https://doi.org/https://doi.org/10.1016/j.ensm.2019.12.033>.
- (16) Furuse, S.; Brattås, L.; Kjekshus, A.; Andresen, A. F.; Fischer, P. On the Crystal Structures of  $\text{TiS}_3$ ,  $\text{ZrS}_3$ ,  $\text{ZrSe}_3$ ,  $\text{ZrTe}_3$ ,  $\text{HfS}_3$ , and  $\text{HfSe}_3$ . *Acta Chem. Scand* 623–631.
- (17) Gorocho, O.; Katty, A.; Le Nagard, N.; Levy-Clement, C.; Schleich, D. M. Photoelectrochemical Study of  $\text{TiS}_3$  in Aqueous Solution. *Mater. Res. Bull.* **1983**, *18* (1), 111–118. [https://doi.org/https://doi.org/10.1016/0025-5408\(83\)90178-2](https://doi.org/https://doi.org/10.1016/0025-5408(83)90178-2).
- (18) Buerger, M. J. Interatomic Distances in Marcasite and Notes on the Bonding in Crystals of Löllingite, Arsenopyrite, and Marcasite Types. *Zeitschrift für Krist. - Cryst. Mater.* **97** (1), 504–513. <https://doi.org/https://doi.org/10.1524/zkri.1937.97.1.504>.
- (19) Folmer, J. C. W.; Jellinek, F.; Calis, G. H. M. The Electronic Structure of Pyrites, Particularly  $\text{CuS}_2$  and  $\text{Fe}_{1-x}\text{Cu}_x\text{Se}_2$ : An XPS and Mössbauer Study. *J. Solid State Chem.* **1988**, *72* (1), 137–144. [https://doi.org/https://doi.org/10.1016/0022-4596\(88\)90017-5](https://doi.org/https://doi.org/10.1016/0022-4596(88)90017-5).
- (20) Li, B.; Jiang, N.; Huang, W.; Yan, H.; Zuo, Y.; Xia, D. Thermodynamic Activation of Charge Transfer in Anionic Redox Process for Li-Ion Batteries. *Adv. Funct. Mater.* **2018**, *28* (4), 1704864. <https://doi.org/https://doi.org/10.1002/adfm.201704864>.
- (21) Saha, S.; Assat, G.; Sougrati, M. T.; Foix, D.; Li, H.; Vergnet, J.; Turi, S.; Ha, Y.; Yang, W.; Cabana, J.; Rousse, G.; Abakumov, A. M.; Tarascon, J.-M. Exploring the Bottlenecks of Anionic Redox in Li-Rich Layered Sulfides. *Nat. Energy* **2019**, *4* (11), 977–987. <https://doi.org/10.1038/s41560-019-0493-0>.
- (22) Sakuda, A.; Takeuchi, T.; Okamura, K.; Kobayashi, H.; Sakaebe, H.; Tatsumi, K.; Ogumi, Z. Rock-Salt-Type Lithium Metal Sulphides as Novel Positive-Electrode Materials. *Sci. Rep.* **2014**, *4* (1), 4883. <https://doi.org/10.1038/srep04883>.
- (23) Leube, B. T.; Robert, C.; Foix, D.; Porcheron, B.; Dedryvère, R.; Rousse, G.; Salager, E.; Cabelguen, P.-E.; Abakumov, A. M.; Vezin, H.; Doublet, M.-L.; Tarascon, J.-M. Activation of Anionic Redox in  $d^0$  Transition Metal Chalcogenides by Anion Doping. *Nat. Commun.* **2021**, *12* (1), 5485. <https://doi.org/10.1038/s41467-021-25760-8>.
- (24) Leube, B. T.; Suard, E. Structure Solution of Novel Na-Ti-S Phase. Institut Laue-Langevin (ILL). **2021**. <https://doi.org/10.5291/ILL-DATA.EASY-873>.
- (25) Lissner, F.; Schleid, T.  $\text{Na}_2\text{ZrS}_3$ : Ein Ternäres Sulfid Des Zirconiums Mit Aufgefüllter  $\text{AlCl}_3$ -Struktur. *Zeitschrift für Anorg. und Allg. Chemie* **1999**, *625* (2), 195–196. [https://doi.org/https://doi.org/10.1002/\(SICI\)1521-3749\(199902\)625:2<195::AID-ZAAC195>3.0.CO;2-V](https://doi.org/https://doi.org/10.1002/(SICI)1521-3749(199902)625:2<195::AID-ZAAC195>3.0.CO;2-V).
- (26) Harringer, N. A.; Kolb, A.; Klepp, K. O.  $\text{Na}_2\text{ZrSe}_3$ , Ein Neues Chalcogenometallat(IV) Mit Schichtstruktur/ $\text{Na}_2\text{ZrSe}_3$ , a New Chalcogenometallate(IV) with a Layered Structure. *Zeitschrift für Naturforsch. B* **2001**, *56* (12), 1322–1324. <https://doi.org/doi:10.1515/znb-2001-1212>.
- (27) Liu, J.; Yin, L.; Wu, L.; Bai, J.; Bak, S.-M.; Yu, X.; Zhu, Y.; Yang, X.-Q.; Khalifah, P. G. Quantification of Honeycomb Number-Type Stacking Faults: Application to  $\text{Na}_3\text{Ni}_2\text{BiO}_6$  Cathodes for Na-Ion Batteries. *Inorg. Chem.* **2016**, *55* (17), 8478–8492. <https://doi.org/10.1021/acs.inorgchem.6b01078>.
- (28) Saha, S. Exploration of Ionic Conductors and Li-Rich Sulfides for All-Solid-State Batteries, 2020.

- (29) Martinolich, A. J.; Zak, J. J.; Agyeman-Budu, D. N.; Kim, S. S.; Bashian, N. H.; Irshad, A.; Narayan, S. R.; Melot, B. C.; Nelson Weker, J.; See, K. A. Controlling Covalency and Anion Redox Potentials through Anion Substitution in Li-Rich Chalcogenides. *Chem. Mater.* **2021**, *33* (1), 378–391. <https://doi.org/10.1021/acs.chemmater.0c04164>.
- (30) Chianelli, R. R.; Dines, M. B. Reaction of Butyllithium with Transition Metal Trichalcogenides. *Inorg. Chem.* **1975**, *14* (10), 2417–2421. <https://doi.org/10.1021/ic50152a023>.
- (31) Ōnuki, Y.; Inada, R.; Tanuma, S.; Yamanaka, S.; Kamimura, H. Electrochemical Characteristics of Transition-Metal Trichalcogenides in the Secondary Lithium Battery. *Solid State Ionics* **1983**, *11* (3), 195–201. [https://doi.org/https://doi.org/10.1016/0167-2738\(83\)90024-3](https://doi.org/https://doi.org/10.1016/0167-2738(83)90024-3).
- (32) Holleck, G. L.; Driscoll, J. R. Transition Metal Sulfides as Cathodes for Secondary Lithium Batteries—II. Titanium Sulfides. *Electrochim. Acta* **1977**, *22* (6), 647–655. [https://doi.org/https://doi.org/10.1016/0013-4686\(77\)85134-7](https://doi.org/https://doi.org/10.1016/0013-4686(77)85134-7).
- (33) Murphy, D. W.; Trumbore, F. A. The Chemistry of  $\text{TiS}_3$  and  $\text{NbSe}_3$  Cathodes. *J. Electrochem. Soc.* **1976**, *123* (7), 960–964. <https://doi.org/10.1149/1.2133012>.
- (34) Murphy, D. W.; Trumbore, F. A. Metal Chalcogenides as Reversible Electrodes in Nonaqueous Lithium Batteries. *J. Cryst. Growth* **1977**, *39* (1), 185–199. [https://doi.org/https://doi.org/10.1016/0022-0248\(77\)90165-8](https://doi.org/https://doi.org/10.1016/0022-0248(77)90165-8).
- (35) Huang, F. Q.; Yao, J.; Liu, Z.; Yang, J.; Ibers, J. A. Synthesis, Structure, and Ionic Conductivity of  $\text{Na}_5\text{Li}_3\text{Ti}_2\text{S}_8$ . *J. Solid State Chem.* **2008**, *181* (4), 837–841. <https://doi.org/https://doi.org/10.1016/j.jssc.2008.01.023>.
- (36) House, R. A.; Maitra, U.; Pérez-Osorio, M. A.; Lozano, J. G.; Jin, L.; Somerville, J. W.; Duda, L. C.; Nag, A.; Walters, A.; Zhou, K.-J.; Roberts, M. R.; Bruce, P. G. Superstructure Control of First-Cycle Voltage Hysteresis in Oxygen-Redox Cathodes. *Nature* **2020**, *577* (7791), 502–508. <https://doi.org/10.1038/s41586-019-1854-3>.
- (37) Dorrian, J. F.; Newnham, R. E. Refinement of the Structure of  $\text{Li}_2\text{TiO}_3$ . *Mater. Res. Bull.* **1969**, *4* (3), 179–183. [https://doi.org/https://doi.org/10.1016/0025-5408\(69\)90054-3](https://doi.org/https://doi.org/10.1016/0025-5408(69)90054-3).
- (38) Meng, F.; Liu, Y.; Xue, T.; Su, Q.; Wang, W.; Qi, T. Structures, Formation Mechanisms, and Ion-Exchange Properties of  $\alpha$ -,  $\beta$ -, and  $\gamma$ - $\text{Na}_2\text{TiO}_3$ . *RSC Adv.* **2016**, *6* (113), 112625–112633. <https://doi.org/10.1039/C6RA16984H>.



# **The layered sodium titanium trichalcogenide $\text{Na}_2\text{TiCh}_3$ framework ( $\text{Ch} = \text{S, Se}$ ): A rich crystal and electrochemical chemistry.**

Bernhard T. Leube<sup>1,2</sup>, Elodie Salager<sup>2,3</sup>, Erwan Chesneau<sup>2,3</sup>, Gwenaëlle Rousse<sup>1,2,4</sup>, Hervé Vezin<sup>5</sup>, Artem M. Abakumov<sup>6</sup> and Jean-Marie Tarascon<sup>1,2</sup>

<sup>1</sup> Collège de France, Chaire de Chimie du Solide et de l'Energie, UMR 8260, 11 Place Marcelin Berthelot, 75231 CEDEX 05 Paris, France

<sup>2</sup> Réseau sur le Stockage Electrochimique de l'Energie (RS2E), FR CNRS 3459, 33 Rue Saint Leu, 80039 Amiens, France

<sup>3</sup> CNRS, CEMHTI, UPR3079, Université d'Orléans, 1D avenue de la recherche scientifique, Orléans, France

<sup>4</sup> Sorbonne Université, 4 Place Jussieu, F-75005 Paris, France

<sup>5</sup> Université Lille Nord de France, CNRS UMR8516, LASIRE, Villeneuve d'Ascq, France

<sup>6</sup> Center for Energy Science and Technology, Skolkovo Institute of Science and Technology, Nobel str. 3, 121205 Moscow, Russia

# Synthesis.

**General procedure.** Due to the water/air sensitivity of sulfides, all sample manipulations were executed in glove boxes. The commercially available reagents  $\text{TiS}_2$  (Sigma-Aldrich, 99.9%) and  $\text{Na}_2\text{S}$  (Sigma-Aldrich) were used as received from the vendors. All other reagents ( $\text{Li}_2\text{S}$ ,  $\text{Na}_2\text{Se}$ ,  $\text{TiSe}_2$ ,  $\text{ZrS}_2$  and  $\text{ZrSe}_2$ ) were synthesized in-house as described in the following section. The title compounds  $\text{Na}_{2-x}\text{Li}_x\text{TiS}_3$  ( $x = 0, 0.5, 1.0, 1.5$ ) and  $\text{Na}_2\text{TMCh}_3$  ( $\text{TM} = \text{Ti, Zr}; \text{Ch} = \text{S, Se}$ ) were prepared by hand-grinding the reagents in appropriate stoichiometric ratios, consecutive sealing in evacuated quartz tubes under vacuum ( $p < 10^{-4}$  mbar) as powder and high-temperature calcination. The appropriate heating temperature  $T$  and time  $t$  were investigated for each targeted composition, giving the following optimized parameters (*n. b.* the minimal time  $t$  necessary for full completion of the reaction was not subject of the optimization):

	Temperature $T$ / K	Time $t$ / h
$\text{Na}_2\text{TiS}_3$	773	48
$\text{Na}_{1.5}[\text{Li}_{0.5}\text{Ti}]\text{S}_3$	773	36
$\text{Na}_2\text{TiSe}_3$	673	36
$\text{Na}_2\text{ZrS}_3$	973	72
$\text{Na}_2\text{ZrSe}_3$	773	72

**$\text{Li}_2\text{S}$ .** Lithium sulfide was synthesized by heating lithium carbonate ( $\text{Li}_2\text{CO}_3$ , Sigma-Aldrich, > 99%) under a stream of argon/ $\text{CS}_2$  (Sigma-Aldrich) vapor at 923 K for 5 h.

**$\text{Na}_2\text{Se}$ .** Sodium selenide was synthesized by mechanically mixing Na metal and Se powder using a Fritsch pulverisette 7 planetary ball mill (typically 3g, 10 10-mm  $\text{ZrO}_2$  balls in a 80 mL  $\text{ZrO}_2$  jar, 10 h, 500 rpm).

**$\text{TiSe}_2$ .** Titanium selenide was synthesized by heating titanium (Ti, Sigma-Aldrich, 99.98%) and selenium powder (Se, Alfa Aesar, 99.999%) in an evacuated quartz tube at 673 K for 12 h.

**$\text{ZrCh}_2$  ( $\text{Ch} = \text{S, Se}$ ).** Zirconium chalcogenides were synthesized by heating zirconium wire (Zr, Alfa Aesar, 99.2%) with sulphur (S, Sigma-Aldrich, 99.98%) or selenium powder at 1273 K for 12 h applying a very low heating rate of 0.5 K/min.

**Chemical desodiation of  $\text{Na}_2\text{TiS}_3$ .**  $\text{Na}_2\text{TiS}_3$  (100 mg, 0.526 mmol) and iodine ( $\text{I}_2$ , 133.6 mg, 0.626 mmol, 1.2 eq) were dispersed in 10 mL Acetonitrile and stirred at ambient temperature for 20 h. The reaction product  $\text{Na}_x\text{TiS}_3$  was separated by centrifugation, washed with Acetonitrile (3x 10 mL) and finally dried under vacuum.

**$\text{Na}_{1.5}[\text{Li}_{0.5}\text{Ti}]\text{O}_3$ .**  $\text{Li}_2\text{CO}_3$  (276.1 mg, 3.74 mmol, Sigma, > 99%),  $\text{Na}_2\text{CO}_3$  (1188.0 mg, 11.2 mmol, Alfa Aesar, 99%) and  $\text{TiO}_2$  (Anatase, 1193.6 mg, 14.95 mmol, Alfa Aesar, nanopowder, > 99.7%) were thoroughly hand ground in a pestle and mortar and calcined in an alumina crucible at 923 K for 12 h.

## Characterization.

**X-ray powder diffraction.** High resolution synchrotron X-ray diffraction (SXR) patterns were recorded at the Cristal beamline of the Soleil synchrotron ( $\lambda = 0.58185 \text{ \AA}$ ) or at the 11-BM of the Advanced Photon Source (APS), Argonne National Laboratory ( $\lambda = 0.457889 \text{ \AA}$ ). The samples were sealed in quartz capillaries ( $r_{\text{cap}} = 0.3 \text{ mm}$ ) and measured in transmission mode. For in house powder X-ray diffraction (PXRD) experiments samples were enclosed in an airtight electrochemical cell with a Be window. The data was collected in reflection mode in Bragg-Brentano geometry using a Bruker D8 Advance diffractometer equipped with a Cu-K $\alpha$  source ( $\lambda_1 = 1.54056 \text{ \AA}$ ,  $\lambda_2 = 1.54439 \text{ \AA}$ ) and a LynxEye detector. Analysis and refinements of the as collected diffraction patterns were carried out using the FullProf program suite.

**Neutron powder diffraction.** A constant wavelength neutron powder diffraction (NPD) pattern of approximately 1.7 g pristine Na<sub>2</sub>TiS<sub>3</sub> was recorded on the D2B diffractometer, Institut Laue-Langevin, while 2 g of pristine Na<sub>1.5</sub>[Li<sub>0.5</sub>Ti]S<sub>3</sub> was measured on the Echidna diffractometer, ANSTO (Australian Nuclear Science and Technology Organisation).

**Electrochemical characterization.** To prepare the cathode active material Na<sub>2-x</sub>Li<sub>x</sub>TmCh<sub>3</sub> (Tm= Ti, Zr; Ch= S, Se) was thoroughly mixed and ground with 15 wt% conductive carbon (Csp). Typical Swagelok-type cells with loadings of 5-10 mg of the cathode material, Whatman GF/D borosilicate glass fiber membranes as the separator, electrolyte (250-500  $\mu\text{L}$ ) and a metallic anode were assembled in an Ar-filled glovebox. For cycling against Li, Li ribbon was used as the anode in combination with LP30 as the electrolyte (1 M LiPF<sub>6</sub> in dimethylcarbonate/ethylenecarbonate (1:1)). In the case of cycling against Na, metallic Na was used as the anode with 1 M NaPF<sub>6</sub> in propylenecarbonate as the electrolyte. The cells were allowed to rest for 30 min and were then galvanostatically cycled at C/10 rate, corresponding to the removal of 1 Li per formula unit in 10h. For *ex-situ* experiments the cathode materials were recovered after cycling, washed with dimethylcarbonate (DMC, Sigma-Aldrich, >99%) and dried under vacuum. Galvanostatic intermittent titration technique (GITT) experiments were run on the second electrochemical cycle of the respective material with galvanostatic pulses at rates of C/10 for 1.5 h followed by a 4 h open circuit step.

**EPR.** Room temperature and 110K X-Band EPR measurement were performed with a Bruker ELEXSYS E500. The spectra were recorded with 5mW microwave power and 2 G for amplitude modulation.

**TEM.** TEM samples were prepared by dispersing the powder in DMC (dimethyl carbonate) in an agate mortar and depositing drops of this suspension onto a carbon film supported by a copper grid. The samples were transferred from the Ar-filled glove box to the microscope column using a Gatan vacuum transfer holder completely excluding contact with air. Electron diffraction (ED) patterns, high-angle annular dark-field scanning transmission electron microscopy (HAADF-STEM) images and scanning transmission electron microscopy (STEM-EDX) compositional maps were acquired on a probe aberration-corrected Titan Themis Z electron microscope operated at 200 kV and equipped with a Super-X system for energy-dispersive X-ray (EDX) analysis.

**NMR.** <sup>23</sup>Na NMR experiments for the Na<sub>2</sub>TiS<sub>3</sub> pristine, charged and discharged (against Li<sup>+</sup>/Li) samples were conducted using a Bruker Avance III with a magnetic field of 4.7 T to increase the quadrupolar effect on the spectrum and better separate the sites. The spectra display signals with quadrupolar lineshapes that constrain the fits better. The NMR spectra were recorded using a Bruker 1.3 mm double resonance HX Bruker MAS probe spinning the rotors at the magic angle at a rate of 62.5 kHz. RF nutation was strongly influenced by the quadrupolar interaction; a strong and short pulse was used for quantitativity ( $\pi/18$  at 50 W). The repetition time was adapted to be longer than 5 times the

longitudinal relaxation time and the number of co-added transients was 348, 8192 and 4096, for respectively. For  $\text{Na}_{1.5}\text{Li}_{0.5}\text{TiS}_3$  2240 transients were coadded. (Figure 8a,b,e).

The quantification of the  $^{23}\text{Na}$  NMR for the  $\text{Na}_{1.5}\text{Li}_{0.5}\text{TiS}_3$  series (pristine, charged and discharged) was conducted on a Bruker Avance III with a magnetic field of 17.6 T, using a Bruker 1.3 mm double resonance HX MAS probe. The rotor for the charged sample could not be spun faster than 60 kHz hence all samples were measured at that spinning rate. Pi/18 pulses were used at 30 W (87 kHz on the liquid reference) and the repetition time was adjusted to ensure quantitativity. 128 or 384 transients were coadded. The spectra were referenced to a  $1 \text{ mol}\cdot\text{L}^{-1}$  aqueous NaCl solution at 0 ppm (Figure 8f).

The  $^7\text{Li}$  NMR spectra of all samples (Figure 8g,h) were recorded in the high-field spectrometers, using the same Bruker 1.3 mm HX probe, with a single pulse at 30 W (102 kHz on the liquid reference no quadrupolar effect detected). The spectra were processed with an exponential apodization (line broadening of 5 Hz) and referenced to a  $1 \text{ mol}\cdot\text{L}^{-1}$  aqueous LiCl solution at 0 ppm.

A home-made MATLAB script (MathWorks) was used to open the data and integrate the  $^{23}\text{Na}$  and  $^7\text{Li}$  NMR spectra. The central transition and the  $n=0$  band of the satellite transitions were integrated together, as the broader lines prevent spectral selection. Tests on the pristine materials indicate that it creates an error of  $\sim 2\%$  on the measurements.

We considered that the pristine contained 2 Na and 1.5Na0.5Li per unit formula to calibrate the pristine samples, the other samples were calibrated related to the pristine samples. The areas were corrected for the mass of the sample contained in the rotors.

# Figures

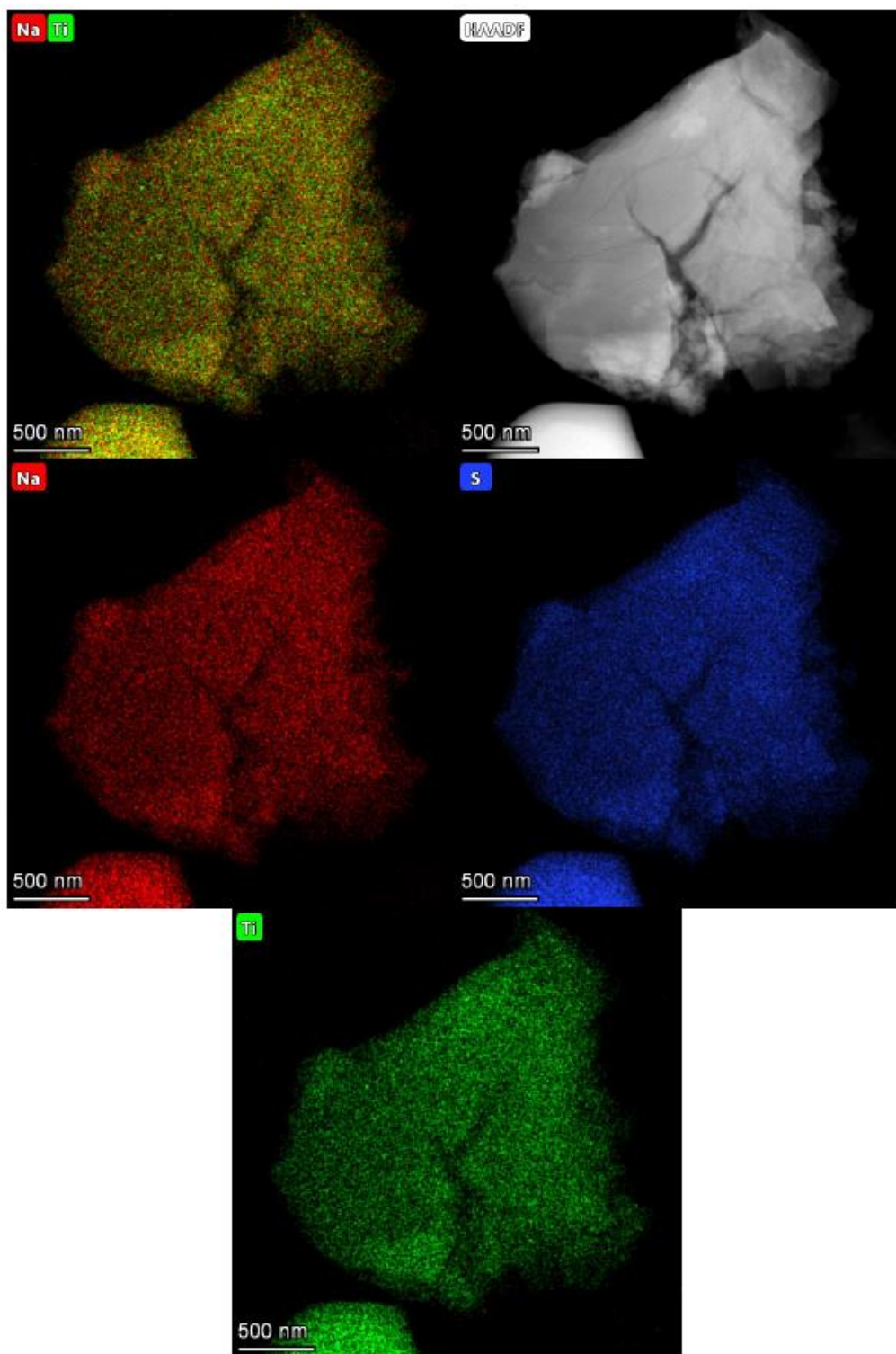


Figure S1: HAADF-STEM image of  $\text{Na}_2\text{TiS}_3$ , the corresponding EDX elemental maps for Na, Ti and S, and the mixed color-coded compositional map.

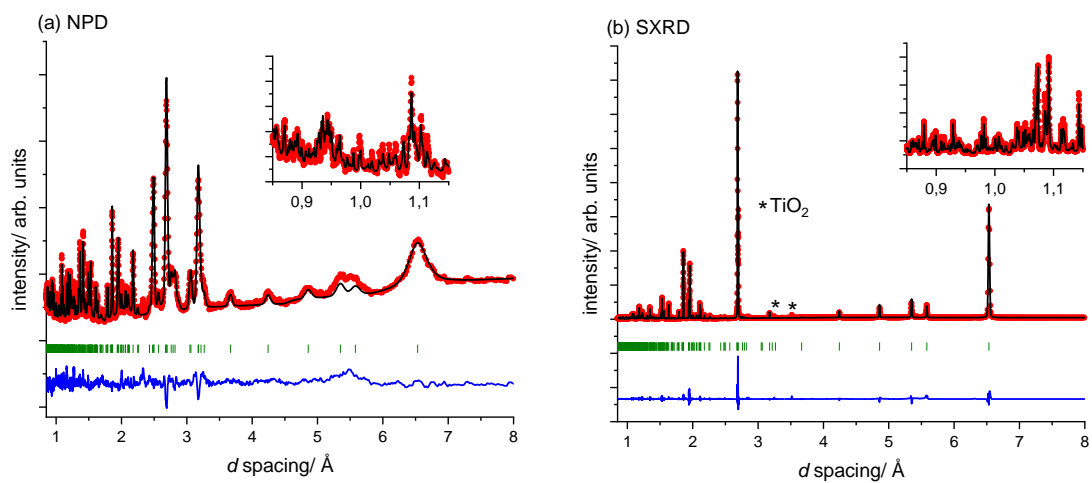


Figure S2: Combined Rietveld refinement of pristine  $\text{Na}_2\text{TiS}_3$  using (a) NPD and (b) SXR data at RT.  $\text{TiO}_2$  impurities are marked by asterisks \*.

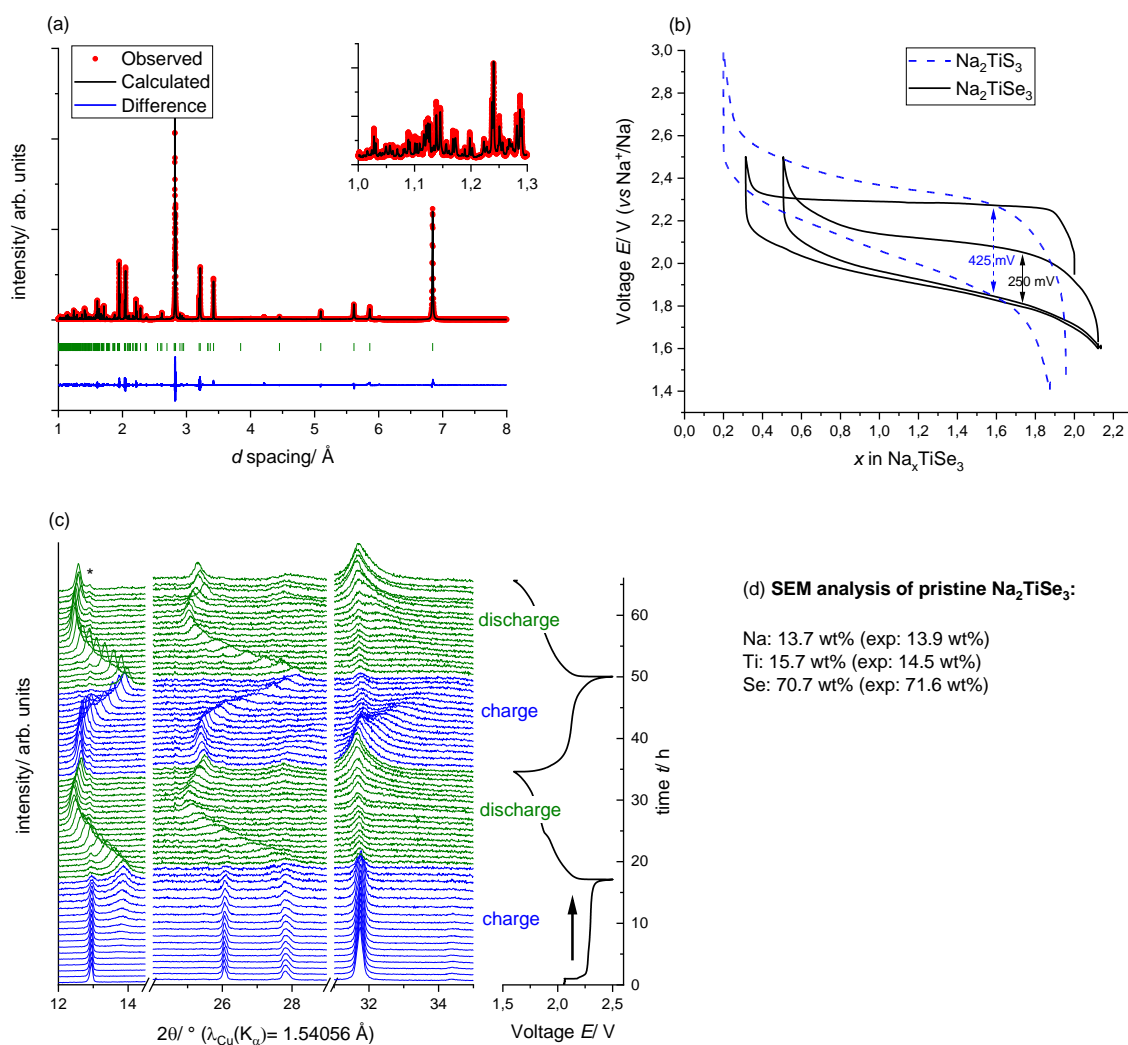


Figure S3: Structural characterization of  $\text{Na}_2\text{TiSe}_3$ : (a) Rietveld refinement based on SXRD data (b) cycled against  $\text{Na}^+/\text{Na}$  (c) operando PXRD experiment vs  $\text{Na}^+/\text{Na}$ , a small amount pristine  $\text{Na}_2\text{TiSe}_3$  was not in electrical contact with the cell and persists throughout the patterns (marked by an asterisk \*). (d) result of a SEM analysis.

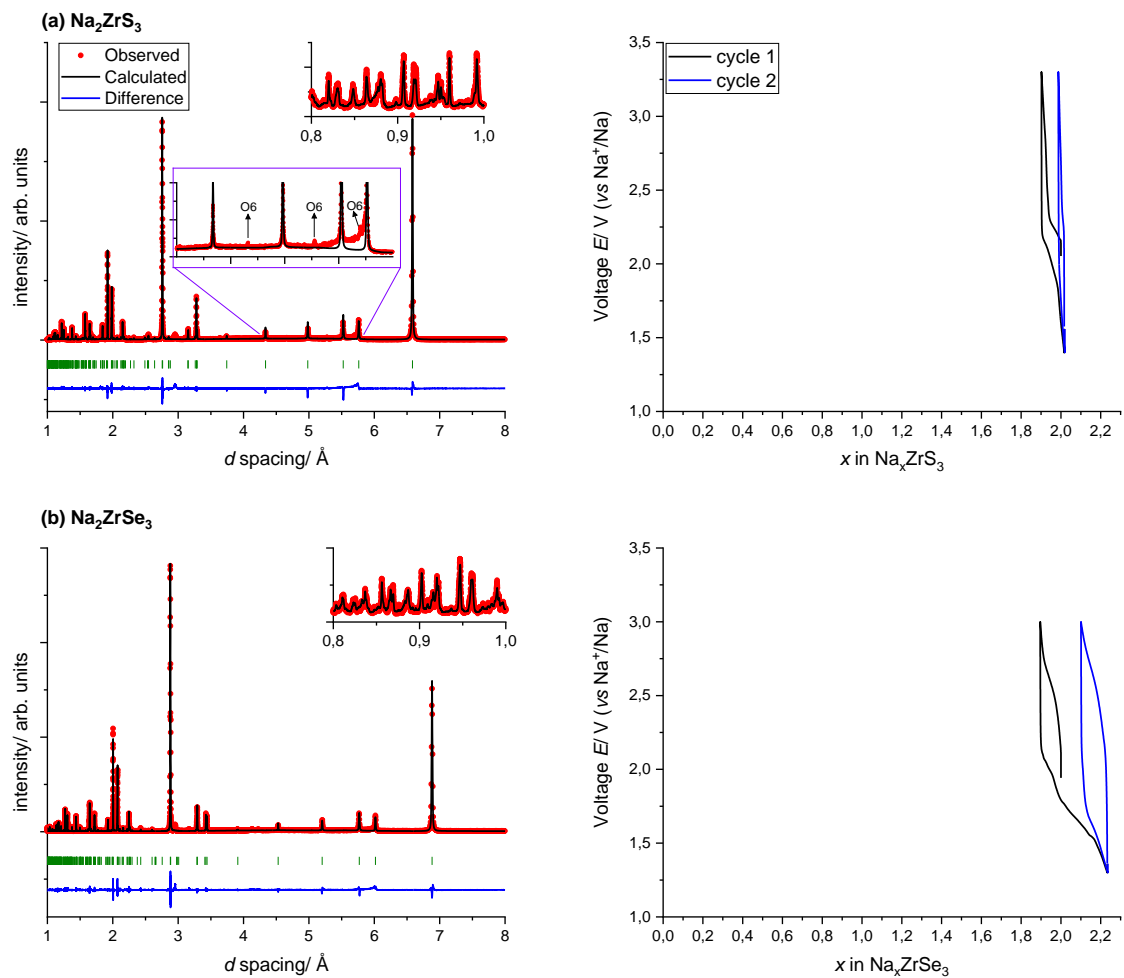


Figure S4: Structure and electrochemistry of (a)  $\text{Na}_2\text{ZrS}_3$  and (b)  $\text{Na}_2\text{ZrSe}_3$ . The structural model of each phase was refined by the Rietveld method using SXRD data.



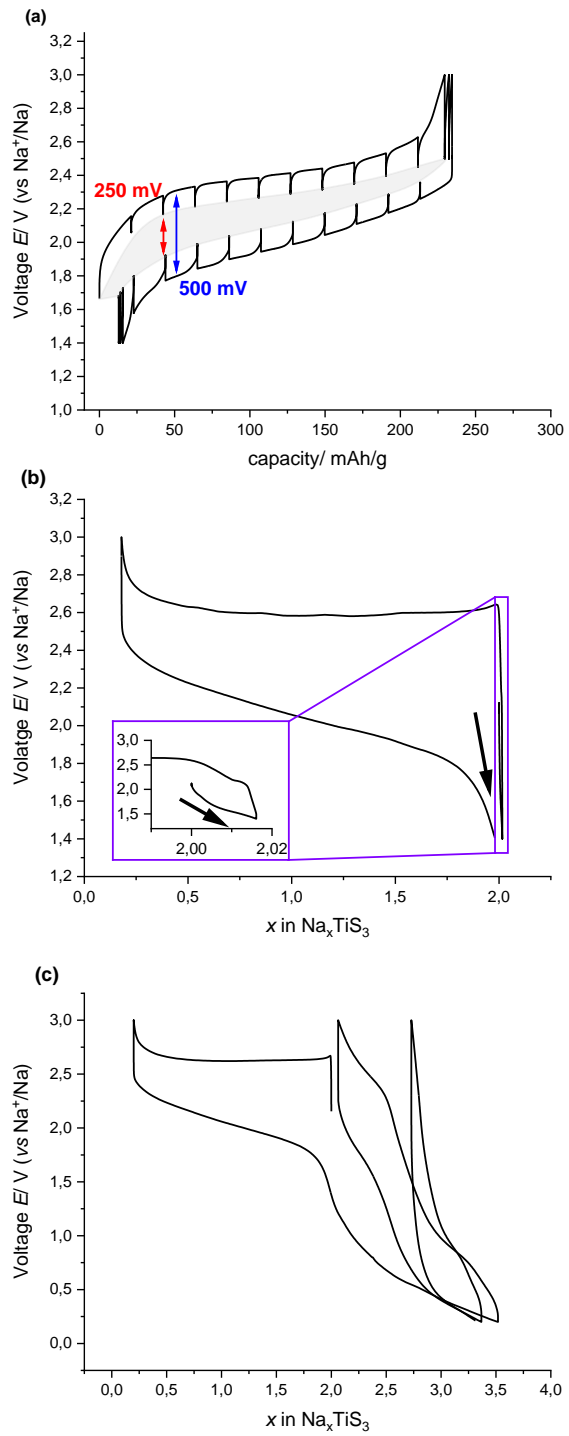


Figure S5: Electrochemistry of  $\text{Na}_2\text{TiS}_3$  vs  $\text{Na}^+/\text{Na}$ . (a) 2<sup>nd</sup> cycle of a GITT experiment (b) cell started on discharge (c) galvanostatic cycling with an increased potential window from 3.0 V- 0.2 V.

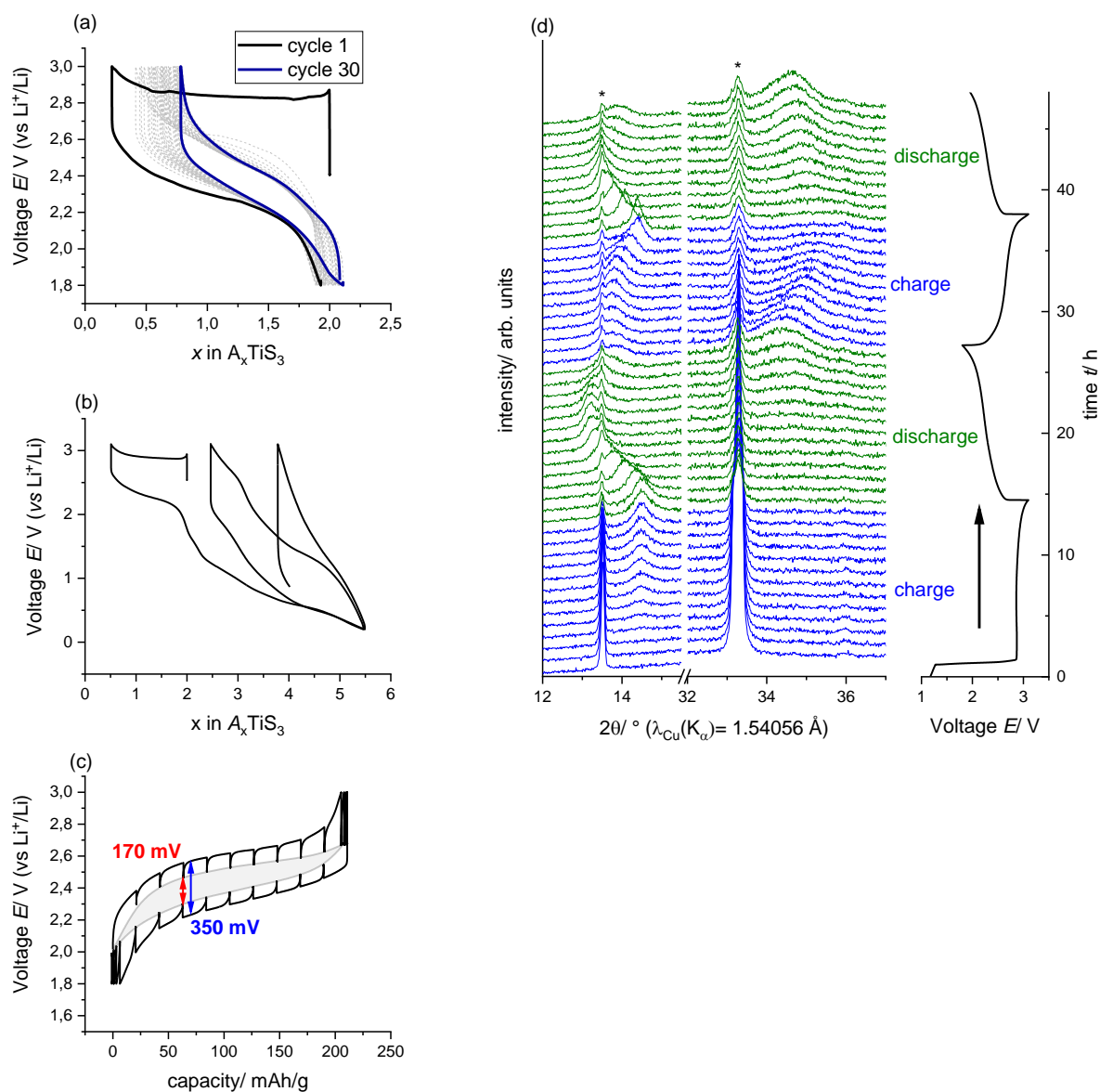


Figure S6: Electrochemical experiments of  $\text{Na}_2\text{TiS}_3$  cycled against  $\text{Li}^+/\text{Li}$  (a) 30 galvanostatic cycles (b)  $\text{Na}_2\text{TiS}_3|\text{Li}$  cell cycled from 3.1 V-0.2 V (c) 2<sup>nd</sup> cycle of a GITT experiment (d) PXRD operando experiment of a  $\text{Na}_2\text{TiS}_3|\text{Li}$  cell, a small amount pristine  $\text{Na}_2\text{TiS}_3$  was not in electrical contact with the cell and persists throughout the patterns (marked by an asterisk \*).

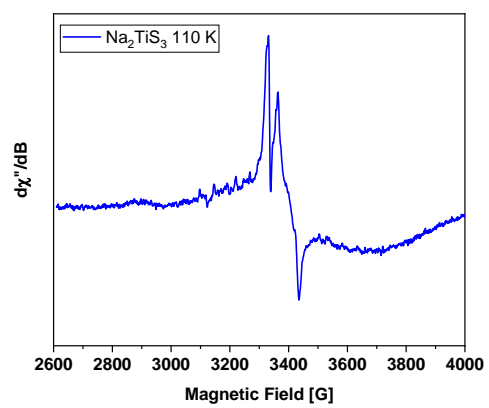
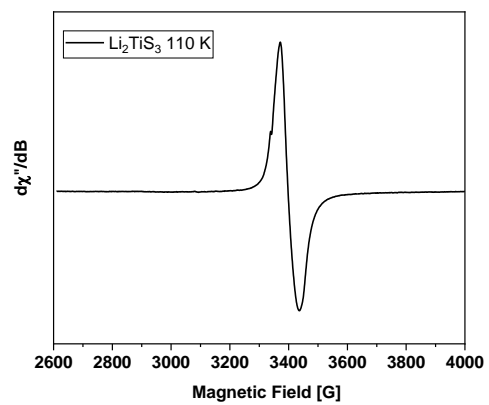


Figure S7: EPR measurement of  $\text{Li}_2\text{TiS}_3$  (black) and  $\text{Na}_2\text{TiS}_3$  (blue) at 110 K.

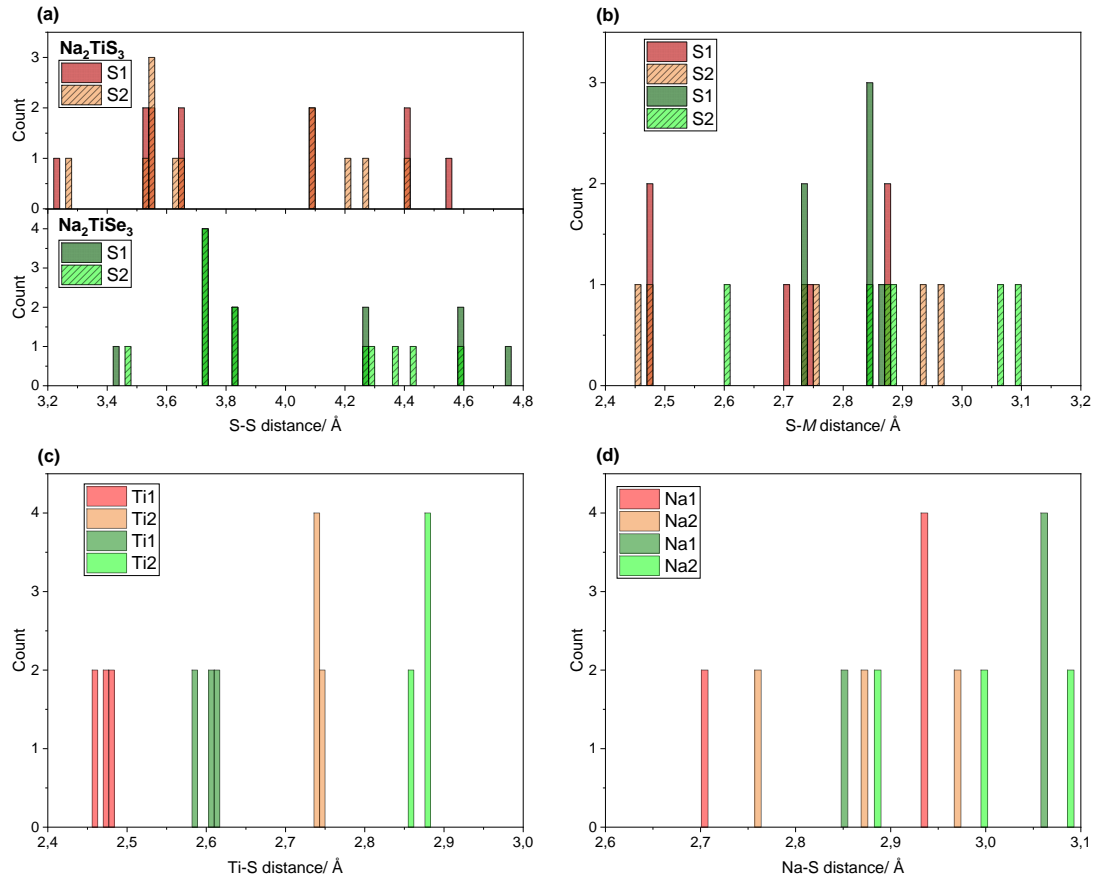


Figure S8 : Analysis of interatomic distances in  $\text{Na}_2\text{TiS}_3$  compared to  $\text{Na}_2\text{TiSe}_3$  based on the Rietveld-refined structures. (a) distance between a given chalcogenide atom in the “cubic” close-packed anion sublattice and its 12 nearest neighbors. (b) bond lengths in a given  $\text{ChM}_6$  octahedron. (c) bond lengths in a given  $\text{MCh}_6$  octahedron. (d) bond lengths in a given  $\text{NaCh}_6$  octahedron. Color code: red:  $\text{Na}_2\text{TiS}_3$ , green:  $\text{Na}_2\text{TiSe}_3$ .

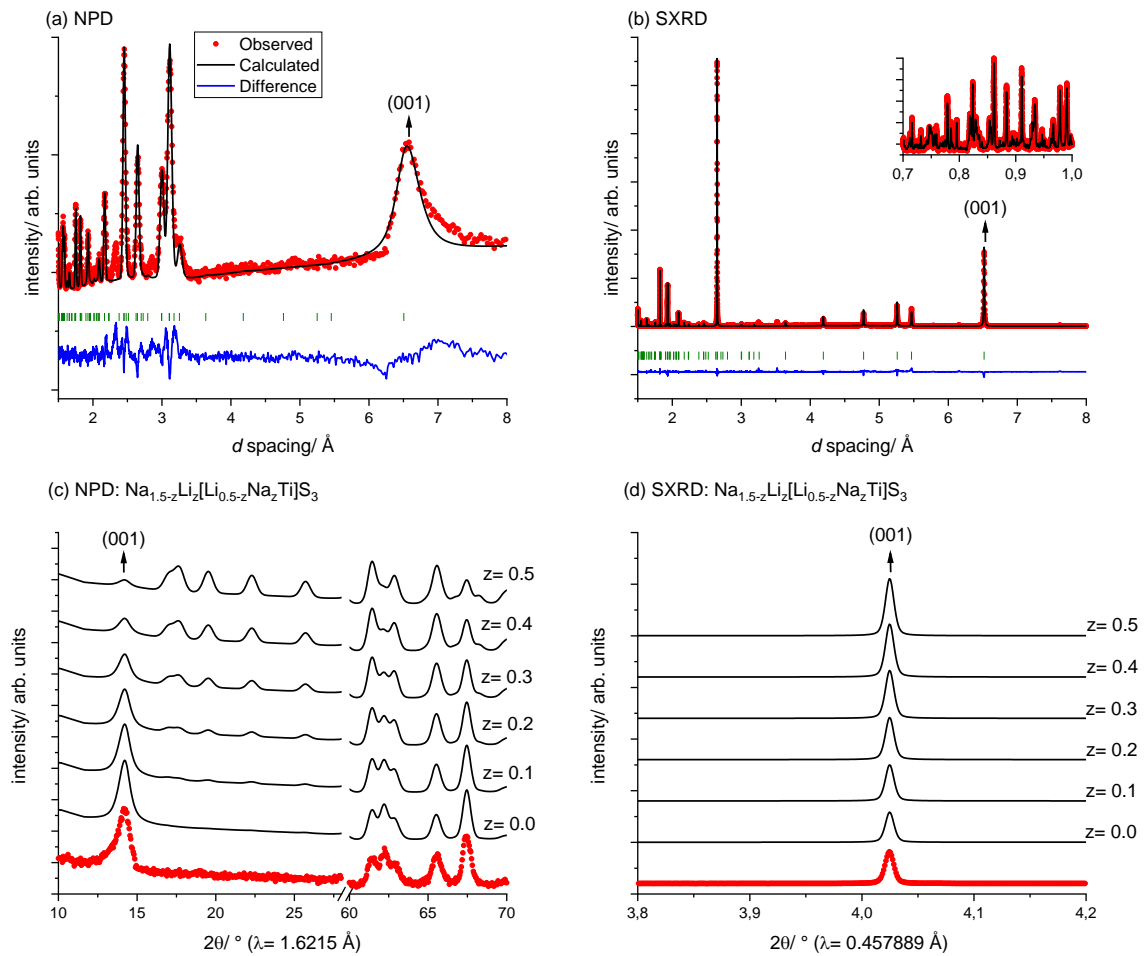


Figure S9: Diffraction experiments on  $\text{Na}_{1.5}[\text{Li}_{0.5}\text{Ti}]\text{S}_3$ . Combined Rietveld refinement of (a) NPD and (b) SXR data. (space group  $R\bar{3}m$ , composition fixed to the nominal stoichiometry). Panels (c) and (d) show simulated NPD and SXR patterns, respectively, for the  $\text{Na}_{1.5-z}\text{Li}_z[\text{Li}_{0.5-z}\text{Na}_z\text{Ti}]\text{S}_3$  series to compare the degree of Li vs Na mixing. The best agreement is observed when Li and Na do not mix at all ( $z=0.0$ ).

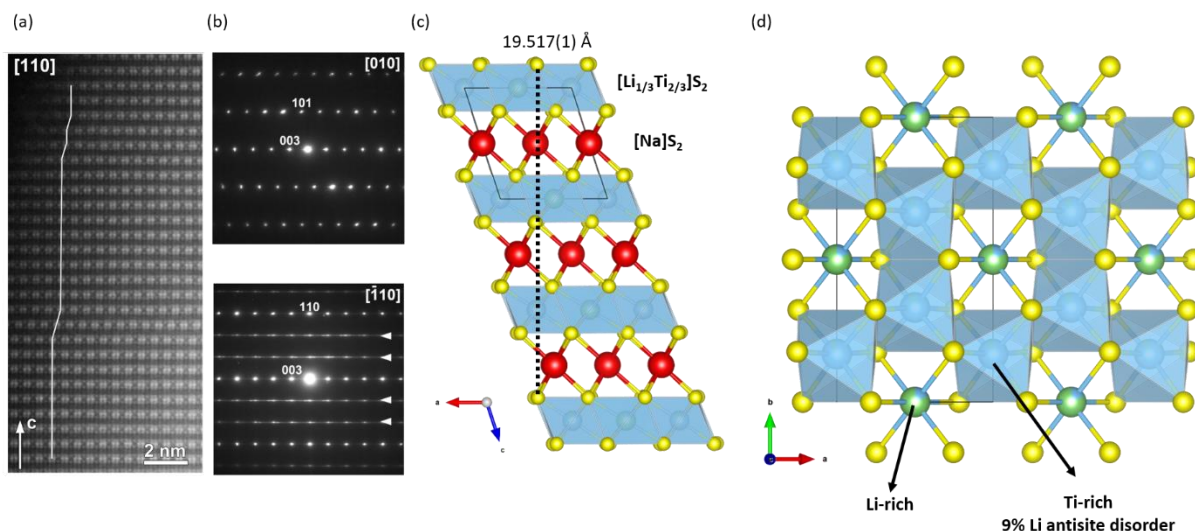


Figure S10: Structural characterization of  $\text{Na}_{1.5}[\text{Li}_{0.5}\text{Ti}]\text{S}_3$ . (a)  $[110]$  HAADF-STEM image, stacking faults along  $c$  are visible by random lateral displacements of the  $[\text{Li}_{1/3}\text{Ti}_{2/3}]\text{S}_2$  blocks traced with zig-zag lines. (b) ED patterns indexed with the  $R\bar{3}m$  space group, extra reflections and diffuse intensity due to the Li-Ti “honeycomb” ordering are marked with arrowheads. (c) structure as obtained from a combined SXR-ED-NPD Rietveld refinement viewed along the  $b$  axis, forming an  $O3$  type structure. (d) Li-Ti “honeycomb” ordering in the mixed  $[\text{Li}_{1/3}\text{Ti}_{2/3}]\text{S}_2$  slabs.

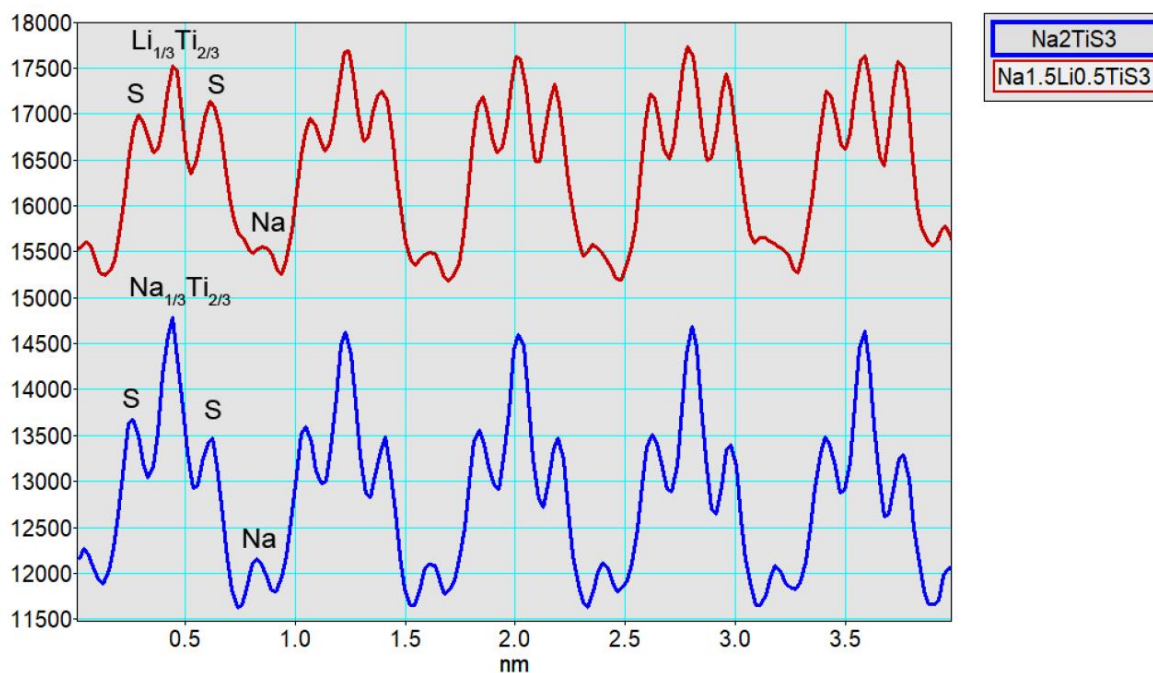


Figure S11: HAADF intensity profiles measured in the  $[010]$  HAADF-STEM image along the  $S\text{-A}_{1/3}\text{Ti}_{2/3}\text{-S}$  columns in the  $\text{Na}_{1.5}\text{Li}_{0.5}\text{TiS}_3$  (red) and  $\text{Na}_2\text{TiS}_3$  (blue) structures. Note the lower HAADF intensity at the  $\text{Li}_{1/3}\text{Ti}_{2/3}$  sites compared to that at the  $\text{Na}_{1/3}\text{Ti}_{2/3}$  ones.

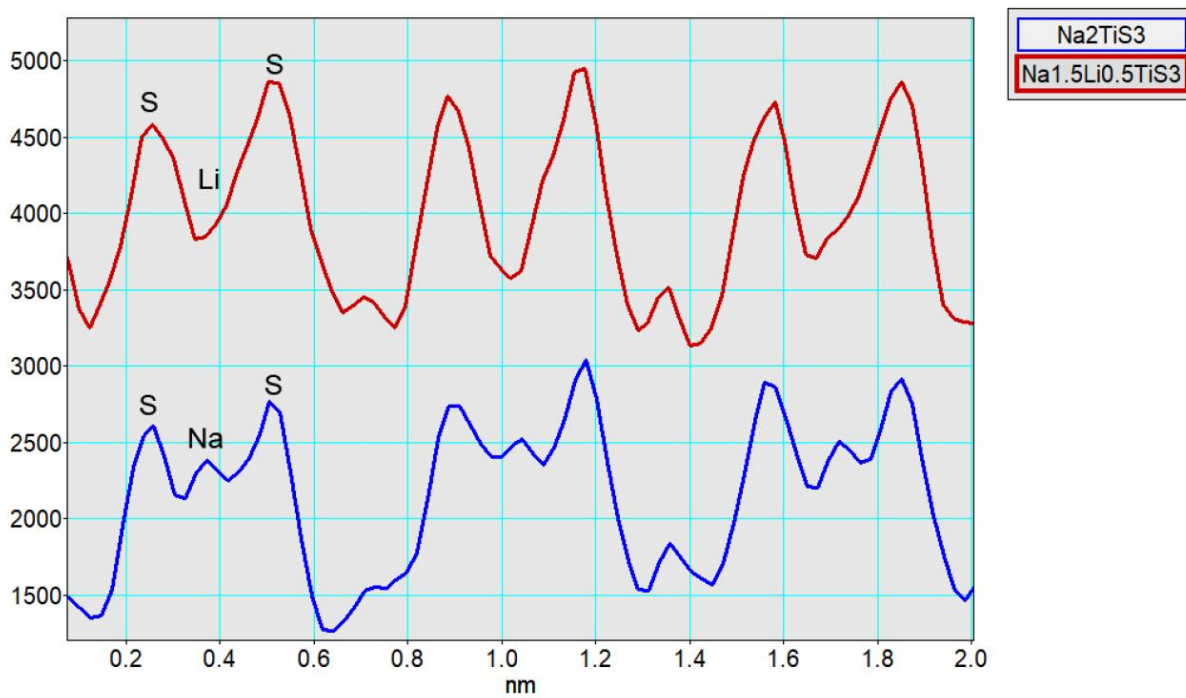


Figure S12: HAADF intensity profiles measured in the [110] HAADF-STEM image along the S-A-S columns in the  $(\text{A}_{1/3}\text{Ti}_{2/3})\text{S}_2$  blocks of the  $\text{Na}_{1.5}\text{Li}_{0.5}\text{TiS}_3$  (red) and  $\text{Na}_2\text{TiS}_3$  (blue) structures. Note the lower HAADF intensity of the A sites occupied by Li compared to those occupied by Na.

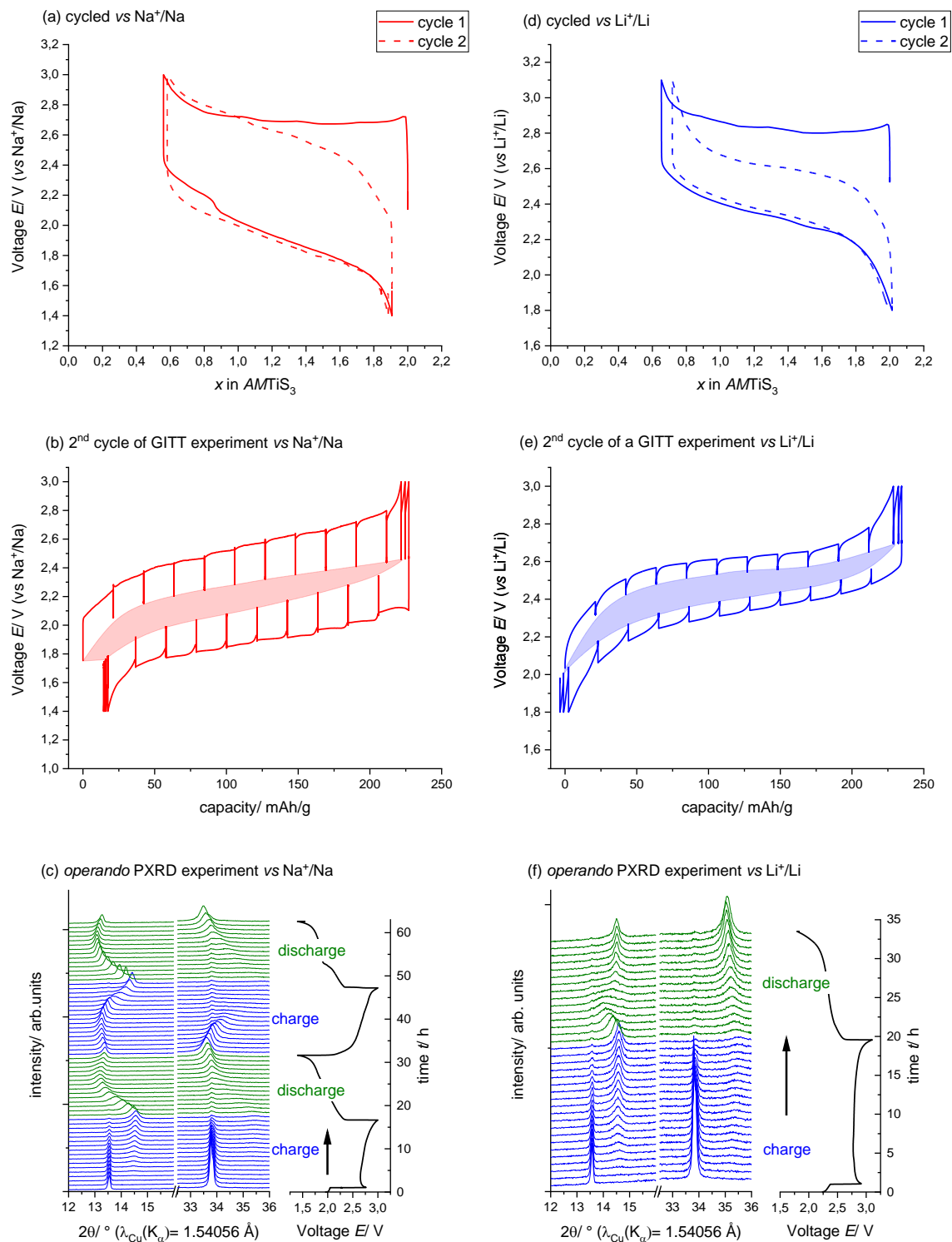


Figure S13: Electrochemistry of  $\text{Na}_{1.5}[\text{Li}_{0.5}\text{Ti}]\text{S}_3$ : Galvanostatic cycling, 2<sup>nd</sup> cycle of a GITT experiment and *operando* PXRD experiment vs  $\text{Na}^+/\text{Na}$  (a)-(c) and vs  $\text{Li}^+/\text{Li}$  (d)-(f) respectively.



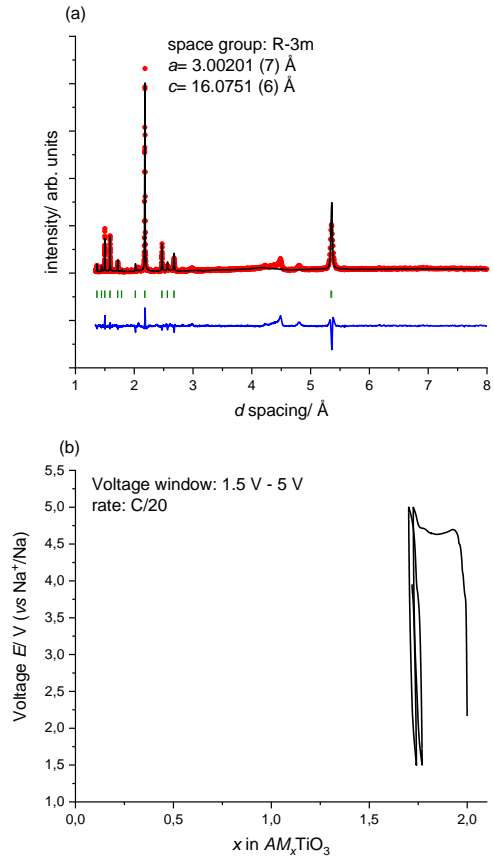


Figure S14: O3 type  $\text{Na}_{1.5}[\text{Li}_{0.5}\text{Ti}]\text{O}_3$ . (a) Pawley fit of  $\text{Na}_{1.5}[\text{Li}_{0.5}\text{Ti}]\text{O}_3$  with the  $R\bar{3}m$  space group. (b) Electrochemical cycling of  $\text{Na}_{1.5}[\text{Li}_{0.5}\text{Ti}]\text{O}_3$  against  $\text{Na}^+/\text{Na}$ .

# Tables

Table S1: Crystallographic data of  $\text{Na}_2\text{TiS}_3$  as obtained from a combined NPD and SXR D Rietveld refinement at 300 K in the  $C2/m$  space group ( $a=6.43018(4)$  Å,  $b=11.16335(7)$  Å,  $c=6.89242(4)$  Å,  $\beta=108.5878(4)^\circ$ ),  $\chi^2(\text{NPD}): 5.58$ ,  $\chi^2(\text{SXR D}): 224.1$ .

Atom	Wyckoff site	$x/a$	$y/b$	$z/c$	$U_{\text{iso}}/\text{Å}^2$	occupancy
S1	4i	0.2033(4)	0	0.2114(4)	0.0173(6)	1
S2	8j	0.2555(3)	0.31668(14)	0.2121(2)	0.0184(4)	1
Ti1	4g	0	0.16821(15)	0	0.0174(5)	0.903(4)
Na1	4g	0	0.16821(15)	0	0.0174(5)	0.097(4)
Ti2	2b	0	0.5	0	0.0180(13)	0.194(8)
Na2	2b	0	0.5	0	0.0180(13)	0.806(8)
Na3	2c	0	0	0.5	0.0238(14)	1
Na4	4h	0	0.3432(3)	0.5	0.0237(9)	1

Table S2: Crystallographic data of  $\text{Na}_2\text{ZrS}_3$  as obtained from SXR D Rietveld refinement in the  $C2/m$  space group ( $a=6.65067(2)$  Å,  $b=11.52461(4)$  Å,  $c=6.95383(2)$  Å,  $\beta=108.7912(2)^\circ$ ),  $\chi^2(\text{SXR D}): 9.9$ .

Atom	Wyckoff site	$x/a$	$y/b$	$z/c$	$U_{\text{iso}}/\text{Å}^2$	occupancy
S1	4i	0.2335(4)	0	0.2229(3)	0.0140(8)	1
S2	8j	0.2491(3)	0.32494(18)	0.2223(2)	0.0190(5)	1
Zr1	4g	0	0.16803(10)	0	0.021281(13)	0.904480(4)
Na1	4g	0	0.16803(10)	0	0.021281(13)	0.095520(4)
Zr2	2b	0	0.5	0	0.01656(4)	0.191041(8)
Na2	2b	0	0.5	0	0.01656(4)	0.808959(8)
Na3	2c	0	0	0.5	0.0201(15)	1
Na4	4h	0	0.3323(4)	0.5	0.0313(10)	1

Table S3: Crystallographic data of  $\text{Na}_2\text{TiSe}_3$  as obtained from SXR D Rietveld refinement in the  $C2/m$  space group ( $a=6.747421(17)$  Å,  $b=11.72281(3)$  Å,  $c=7.219521(17)$  Å,  $\beta=108.59178(16)^\circ$ ),  $\chi^2(\text{SXR D}): 10.1$ .

Atom	Wyckoff site	$x/a$	$y/b$	$z/c$	$U_{\text{iso}}/\text{Å}^2$	occupancy
Se1	4i	0.20673(18)	0	0.21195(18)	0.0214(3)	1
Se2	8j	0.25541(13)	0.31708(6)	0.21511(11)	0.0230(2)	1
Ti1	4g	0	0.16881(19)	0	0.0217(6)	0.87508(6)
Na1	4g	0	0.16881(19)	0	0.0217(6)	0.12492(6)
Ti2	2b	0	0.5	0	0.0292(15)	0.24984(12)
Na2	2b	0	0.5	0	0.0292(15)	0.75016(12)
Na3	2c	0	0	0.5	0.0251(18)	1
Na4	4h	0	0.3430(4)	0.5	0.0318(12)	1

Table S4: Crystallographic data of  $\text{Na}_2\text{ZrSe}_3$  as obtained from SXR D Rietveld refinement in the  $C2/m$  space group ( $a=6.9425(5)$  Å,  $b=12.0342(9)$  Å,  $c=7.2685(5)$  Å,  $\beta=108.74088(19)^\circ$ ),  $\chi^2(\text{SXR D})$ : 9.4.

Atom	Wyckoff site	$x/a$	$y/b$	$z/c$	$U_{\text{iso}}/\text{Å}^2$	occupancy
Se1	4i	0.2206(2)	0	0.2228(2)	0.0190(4)	1
Se2	8j	0.25256(16)	0.32289(7)	0.22372(12)	0.0140(2)	1
Zr1	4g	0	0.16799(12)	0	0.021276(15)	0.8854(17)
Na1	4g	0	0.16799(12)	0	0.021276(15)	0.1146(17)
Zr2	2b	0	0.5	0	0.014020(7)	0.229(3)
Na2	2b	0	0.5	0	0.014020(7)	0.771(3)
Na3	2c	0	0	0.5	0.022(2)	1
Na4	4h	0	0.3385(5)	0.5	0.0319(15)	1

Table S5 : Crystallographic data of the Rietveld refinement of electrochemically discharged  $\text{Na}_2\text{TiS}_3$  in the  $R\bar{3}m$  space group ( $a=3.70249(7)$  Å,  $c=19.8925(4)$  Å),  $\chi^2(\text{SXR D})$ : 16.7.

Atom	Wyckoff site	$x/a$	$y/b$	$z/c$	$U_{\text{iso}}/\text{Å}^2$	occupancy
S1	6c	0	0	0.25872(7)	0.1081(19)	1
Ti1	3a	0	0	0	0.1107(18)	2/3
Na1	3a	0	0	0	0.1107(18)	1/3
Na2	3b	0	0	0	0.074(2)	1

Table S6: Crystallographic data of  $\text{Na}_{1.5}[\text{Li}_{0.5}\text{Ti}]\text{S}_3$  as obtained from a combined NPD and SXR D Rietveld refinement at 300 K in the  $C2/m$  space group ( $a=6.306851(17)$  Å,  $b=10.93529(3)$  Å,  $c=6.853729(15)$  Å,  $\beta=107.9597(2)^\circ$ ),  $\chi^2(\text{NPD})$ : 6.5,  $\chi^2(\text{SXR D})$ : 9.1.

Atom	Wyckoff site	$x/a$	$y/b$	$z/c$	$U_{\text{iso}}/\text{Å}^2$	occupancy
S1	4i	0.2175(3)	0	0.2077(2)	0.0135(5)	1
S2	8j	0.2466(2)	0.32346(12)	0.21081(14)	0.0129(3)	1
Ti1	4g	0	0.16819(13)	0	0.0159(3)	0.9107(13)
Li1	4g	0	0.16819(13)	0	0.0159(3)	0.0893(13)
Ti2	2b	0	0.5	0	0.029(2)	0.179(3)
Li2	2b	0	0.5	0	0.029(2)	0.821(3)
Na3	2c	0	0	0.5	0.0194(10)	1
Na4	4h	0	0.3374(2)	0.5	0.0220(6)	1

Table S7: Overview of phases present in upscale batch of  $\text{Na}_{1.5}[\text{Li}_{0.5}\text{Ti}]\text{S}_3$ .

Material	Detection method	Weight percent
$\text{Na}_{1.5}[\text{Li}_{0.5}\text{Ti}]\text{S}_3$	SXR D	> 94%
$\text{TiO}_2$ (Anatase)	SXR D	< 1%
$\text{TiO}_2$ (Rutile)	SXR D	< 1%
$\text{Na}_5\text{Li}_3\text{Ti}_2\text{S}_8$	SXR D	~ 4%

### Experimental NMR fits (Figure 8a,b in main text)

The spectrum of pristine  $\text{Na}_2\text{TiS}_3$ , processed with an exponential apodization (line broadening of 50 Hz), was fitted in Dmfit,<sup>1</sup> after a spline correction of the baseline, using the INT2QUAD model. The starting parameters if the fit were obtained by fitting a z-filtered MQMAS experiment.<sup>2</sup> Two sites are detected; the first has a relatively symmetric environment ( $C_Q=750$  kHz), the latter has a more distorted environment ( $C_Q=1750$  kHz). A careful integration of the central transition provides an average of 1:3 between the two signals. Based on the integration, we assume that Na#1 corresponds to the Na(1) in the Ti layers while the Na3 and Na4 sites in the Na layers are in exchange, thus resulting in the Na#2 peak.

Table S8: NMR parameters obtained by fitting the  $^{23}\text{Na}$  NMR spectrum of  $\text{Na}_2\text{TiS}_3$ . The chemical shift and quadrupolar tensors are aligned.

Na site	Gaussian Broadening (ppm)	Chemical shift			Quadrupolar interaction	$\eta_Q$	Integration of central transition
		Isotropic shift (ppm) $\delta_{CS}$	Anisotropy (ppm) $\Delta\delta_{CS}$	$\eta_{CS}$			
#1	2.9	9.9	0	0	750	0	25% (0.5 Na)
#2	7.0	12.4	0	0	1800	1	75% (1.5 Na)

The same approach was applied to the  $^{23}\text{Na}$  NMR spectrum of pristine  $\text{Na}_{1.5}\text{Li}_{0.5}\text{TiS}_3$  recorded at 4.7 T. exponential apodization, spline correction of the baseline and starting parameters from a dedicated z-filtered MQ-MAS were used to fit the spectrum in Dmfit. This time the assignment is ambiguous, as 0.5 Li replaced 0.5 Na. The two environments are broader, most probably due to expected enhanced disorder in that phase.

Table S9: NMR parameters obtained by fitting the  $^{23}\text{Na}$  NMR spectrum of  $\text{Na}_{1.5}\text{Li}_{0.5}\text{TiS}_3$ . The chemical shift and quadrupolar tensors are aligned.

Na site	Gaussian Broadening (ppm)	Chemical shift			Quadrupolar interaction	$\eta_Q$	Integration of central transition
		Isotropic shift (ppm) $\delta_{CS}$	Anisotropy (ppm) $\Delta\delta_{CS}$	$\eta_{CS}$			
#1	3.6	8.0	0	0	1480	0.6	55% (0.8 Na)
#2	17.0	9.0	0	0	2260	0.1	45% (0.7 Na)

### CASTEP calculations to confirm assignments (Figure 8c,d)

In order to confirm these assignments and the uncertainties on each, DFT calculations were performed using the CASTEP 20 software<sup>3</sup> with the PBE functional<sup>4</sup> and the on-the-fly pseudopotentials generated by CASTEP. Calculations were performed with a cut-off energy of 600eV and with a tolerance for the convergence of the self-consistent field of  $10^{-7}$ eV. The number of k points was determined in order to have a maximum distance of  $0.04\text{\AA}^{-1}$  between two k points. Input structures were created from CIF files by removing the partial substitutions and converted to CASTEP format using cif2cell program.<sup>5</sup>

Atom's positions of all the structures were optimized by keeping the symmetry operations with an energy's tolerance of  $5 \times 10^{-6}$  eV, a force tolerance of 0.01 eV/Å, and a displacement tolerance of  $5 \times 10^{-4}$  Å. The unit cell parameters were kept fixed at the experimentally determined values.

NMR parameters were calculated using the GIPAW method<sup>6</sup> implemented in CASTEP with the same parameters. In order to compare GIPAW results with experimental spectra in Figure S8 (main text), the spectra were simulated using the DMfit software.<sup>1</sup> The chemical shifts of all sites were referenced in order to match the experimental chemical shift (no prior calibration).

Table S10: NMR parameters for  $\text{Na}_2\text{TiS}_3$  predicted using CASTEP

Na site	Gaussian Broadening (ppm)	Chemical shift			Quadrupolar interaction		Multiplicity
		Isotropic (ppm) $\delta_{\text{CS}}$	Anisotropy (ppm) $\Delta\delta_{\text{CS}}$	Asymmetry $\eta_{\text{CS}}$	Quadrupole coupling constant (kHz) $C_Q$	Assymetry $\eta_Q$	
Na2 (Ti layers)	5.3	9.9	-5.5	0.6	695	0.1	0.5 Na
Na3	5.8	11.6	2.6	0.2	3130	0.2	1 Na
Na4	6.6	13.8	4.5	0.4	1820	0.8	0.5 Na

The calculation on  $\text{Na}_2\text{TiS}_3$  is in relatively good agreement with the experimental data. Na3 is very broad in the static structure. Based on the intensities we hypothesize that we detect all the signals hence Na3 is most probably on exchange with Na4, which results in a smaller quadrupolar effect.

We turn to  $\text{Na}_{1.5}\text{Li}_{0.5}\text{TiS}_3$  to better understand the experimental results. The CASTEP prediction of the shifts is given in Table S4. The partial substitution of Ti by the alkali atoms was removed to simplify the calculation. Two broad signals are predicted, in relatively good agreement with the experimental spectrum, especially if one assumes that the quadrupolar effect is lowered by mobility. This comforts the hypothesis of a layered material with Li in the Ti layers and Na in the S layers.

Table S11: NMR parameters for  $\text{Na}_{1.5}\text{Li}_{0.5}\text{TiS}_3$  predicted using CASTEP.

Na site	Broadening	Chemical shift			Quadrupolar interaction constant (kHz) $C_Q$	Assymetry $\eta_Q$	Multiplicity
		Isotropic (ppm) $\delta_{\text{CS}}$	Anisotropy (ppm) $\Delta\delta_{\text{CS}}$	Asymmetry $\eta_{\text{CS}}$			
Na3	3.8	2.7	4.2	0.7	1335	0.1	1 Na
Na4	11.3	3.8	10.1	0.6	2150	0.0	0.5 Na

# References

- (1) Massiot, D.; Fayon, F.; Capron, M.; King, I.; Le Calvé, S.; Alonso, B.; Durand, J.-O.; Bujoli, B.; Gan, Z.; Hoatson, G. Modelling One- and Two-Dimensional Solid-State NMR Spectra. *Magn. Reson. Chem.* **2002**, *40* (1), 70–76. <https://doi.org/https://doi.org/10.1002/mrc.984>.
- (2) Amoureux, J. P.; Fernandez, C.; Steuernagel, S. Z Filtering in MQMAS NMR. *J. Magn. Reson. Ser. A* **1996**, *123* (1), 116–118. <https://doi.org/DOI 10.1006/jmra.1996.0221>.
- (3) Pickard, C. J.; Mauri, F. All-Electron Magnetic Response with Pseudopotentials: NMR Chemical Shifts. *Phys. Rev. B* **2001**, *63* (24), 245101.
- (4) Perdew, J. P.; Burke, K.; Ernzerhof, M. Generalized Gradient Approximation Made Simple. *Phys. Rev. Lett.* **1996**, *77* (18), 3865–3868. <https://doi.org/DOI 10.1103/PhysRevLett.77.3865>.
- (5) Björkman, T. CIF2Cell: Generating Geometries for Electronic Structure Programs. *Comput. Phys. Commun.* **2011**, *182* (5), 1183–1186.
- (6) Yates, J. R.; Pickard, C. J.; Mauri, F. Calculation of NMR Chemical Shifts for Extended Systems Using Ultrasoft Pseudopotentials. *Phys. Rev. B* **2007**, *76* (2), 24401.